



On the Inference of Tsunami Uncertainties From Landslide Run-Out Observations

T. Zengaffinen-Morris^{1,2}, R. Urgeles³ , and F. Løvholt² 

¹Now at Expert Analytics AS (XAL), Oslo, Norway, ²Norwegian Geotechnical Institute (NGI), Oslo, Norway, ³Institut de Ciències del Mar (CSIC), Barcelona, Spain

Key Points:

- A new landslide database for the Gulf of Cadiz is developed and presented
- Matching a large set of landslide run-outs with a numerical model to provide landslide parameter uncertainties as input to tsunami analysis
- Uncertainty in the tsunami generation is estimated based on constraints from landslide data

Correspondence to:

F. Løvholt,
finn.lovholt@ngi.no

Citation:

Zengaffinen-Morris, T., Urgeles, R., & Løvholt, F. (2022). On the inference of tsunami uncertainties from landslide run-out observations. *Journal of Geophysical Research: Oceans*, 127, e2021JC018033. <https://doi.org/10.1029/2021JC018033>

Received 22 SEP 2021
Accepted 31 MAR 2022

Author Contributions:

Conceptualization: T. Zengaffinen-Morris, F. Løvholt
Formal analysis: T. Zengaffinen-Morris, R. Urgeles
Funding acquisition: F. Løvholt
Investigation: T. Zengaffinen-Morris, R. Urgeles
Methodology: T. Zengaffinen-Morris, R. Urgeles, F. Løvholt
Project Administration: F. Løvholt
Supervision: R. Urgeles, F. Løvholt
Validation: T. Zengaffinen-Morris, R. Urgeles
Visualization: T. Zengaffinen-Morris
Writing – original draft: T. Zengaffinen-Morris, R. Urgeles, F. Løvholt
Writing – review & editing: T. Zengaffinen-Morris, R. Urgeles, F. Løvholt

© 2022. The Authors.

This is an open access article under the terms of the [Creative Commons Attribution-NonCommercial-NoDerivs License](https://creativecommons.org/licenses/by-nc-nd/4.0/), which permits use and distribution in any medium, provided the original work is properly cited, the use is non-commercial and no modifications or adaptations are made.

Abstract Probabilistic tsunami hazard analysis (PTHA) due to submarine landslides is much less developed than PTHA for earthquake sources. This is partly because of less constrained data available for quantifying source probability, and partly because of the lack of knowledge related to the tsunami generation process due to landslide dynamics. This study provides a basis for estimating the uncertainty related to landslide dynamics for PTHA from submarine landslides based on a new landslide database in the Gulf of Cadiz. The establishment of this new database is described herein. We use submarine landslide run-out statistics from this database to calibrate landslide parameters and related uncertainties employing the cohesive landslide model BingClaw. In turn, coupling the landslide motion to tsunami genesis is performed in order to characterize the inferred tsunami uncertainties. Important parameters that can explain the large tsunami uncertainties are the initial water depth of the landslide, the slope, the landslide volume, and the initial yield strength of the landslide material. Kinematic properties such as the initial landslide acceleration or the Froude number are found to strongly correlate with the tsunami-genesis. In this study, we show how matching numerical landslide models with observed run-out from past events in the field can give information about the uncertainty in their tsunami-genic strength. This can in turn be applied in future PTHA for spanning uncertainty ranges due to the landslide dynamics on tsunami-genesis, constrained by landslide run-out data.

Plain Language Summary Investigating tsunami hazard concerns estimating both the impact of a tsunami and its likelihood. Because tsunamis due to submarine landslides are rare, it is difficult to estimate their probability based on historical data. Hence, we need to resort to models to quantify the hazard. To inform such models, calibration against past events is necessary. In this study, we calibrated the landslide models to match run-out of past landslides statistically. We then use the same landslide models to estimate the tsunami-genesis and related uncertainty. Quantifying this uncertainty is a necessary step toward understanding the probability of the tsunami impact.

1. Introduction

Landslides are the second most frequent tsunami source after earthquakes (Harbitz et al., 2014). Arguably, subaerial landslide events, including volcanic flank collapses, represent the most frequent landslide tsunami source, with several significant high runup events occurring in the last decade, including for instance the 2014 Lake Askja (Gylfadóttir et al., 2017; Rauter et al., 2022), the 2015 Taan fjord tsunami (Higman et al., 2018), 2017 Karrat Fjord (Paris et al., 2019; Svennevig et al., 2020), and the 2018 Anak Krakatoa event (Hunt et al., 2021; Walter et al., 2019; Zengaffinen, Løvholt, Pedersen, & Muhari, 2020). Submarine landslide tsunamis are assumed to be less frequent than subaerial landslides, but can involve much larger volumes and hence provide more widespread consequences (Løvholt et al., 2015; Masson et al., 2006). Examples of tsunamigenic submarine landslides include the 8150-year BP Storegga (Bondevik et al., 2005; Kim et al., 2019), the 1929 Grand Banks (Heezen & Ewing, 1952; Løvholt et al., 2018; Piper et al., 1999; Schulten et al., 2019; Zengaffinen, Løvholt, Pedersen, & Harbitz, 2020), the 1979 Lembata Island (Yudhicara et al., 2015), and the 1998 Papua New Guinea (Synolakis et al., 2002; Tappin et al., 2008) events. They sometimes occur contemporaneously with earthquakes that increases the complexity; examples include the 1908 Messina Strait (Favalli et al., 2009; Schambach et al., 2020), 1992 Flores Island (Yeh et al., 1993), and the 2018 Palu (Carvajal et al., 2019; Schambach et al., 2021) events. Further examples can be found in the review of Harbitz et al. (2014).

Despite the presence of several historical submarine landslide tsunamis, it is likely that the occurrence of tsunamis due to submarine landslides in the past is largely under-reported. Morphological observations available from

previous submarine investigations (e.g., Brune et al., 2010; Chaytor et al., 2009; Gamboa et al., 2021, 2022; Geist & ten Brink, 2019; Twichell et al., 2009; Urgeles & Camerlenghi, 2013) reveal occurrence of many large landslides that are likely tsunami-genic due their size (e.g., Løvholt et al., 2017). Most of these landslides have not yet been investigated with respect to their tsunamigenic potential. Conversely, the catalogs reporting these submarine landslide occurrences represent a potential large resource, as they can further help understanding the dynamics of submarine landslide tsunamis, and validate numerical models toward landslide run-out, and when available, tsunami metrics observations. The dynamic information that can be inferred from the landslide source and deposit geometric characterization have previously only been exploited to a limited degree. In past studies (e.g., Gylfadóttir et al., 2017; Kim et al., 2019; Løvholt et al., 2020; Salmanidou et al., 2019, 2017), run-out distances for single landslides and related tsunami observations have been used to calibrate landslide parameters. Related to this, a tsunami sensitivity study has also been previously carried out by Snelling et al. (2020) and Zengaffinen, Løvholt, Pedersen, and Harbitz (2020). Yet, a broader statistical analysis covering variability of different landslides in a whole region has not yet been pursued. Using such a broad data set of past landslides as a basis for testing numerical models can shed light on the uncertainty involved in the landslide processes. As landslide dynamics control this variability, these have in turn first order influence on the tsunami uncertainty.

In this study, statistics of past landslide run-out distances is used to systematically test observations against models and set up constraints for the landslide dynamics and related tsunami probabilities. To this end, we present in the first part of this paper a new submarine landslide database including several hundred events in the Gulf of Cadiz. This database includes matching information of both landslide source area and final run-out distance, and can hence be used as a basis to test numerical landslide models. From this database, we extract landslide run-out statistics as the basis for comparison with landslide models. Here, we attempt to cover the statistical variability of landslides and conditions, across a range of volumes, bathymetric observations, and landslide parameters. Carrying out a high number of numerical landslide simulations is necessary to analyze this variability appropriately. Yet, to enable feasibility, it was deemed necessary to perform the simulations in a simplified geometry. In this study, we carry out the analysis in two horizontal dimensions, which allow for taking into account the aspect ratio of the initial volume configuration of the landslide.

Monte Carlo landslide simulations are used in this paper as input to tsunami simulations. These tsunami simulations are in turn used to produce regression plots visualizing the various degree of data scatter representing uncertainties in the sea surface elevations based on the landslide simulations. Parametric landslide relationships that reduce the tsunami uncertainties are then presented and discussed. The relationships provide an idea of the epistemic uncertainty related to linking landslide dynamics to tsunami-genesis, as informed by the landslide data, and form a basis for future landslide PTHA. To this end, a key finding herein is that bathymetric properties carry a large part of this uncertainty compared to the uncertainty related to the material properties of the landslide. This is also supported by the findings of Snelling et al. (2020), but the range of landslide parameters investigated here is wider.

This paper is organized as follows. In Section 2 the geological setting for the Gulf of Cadiz is provided. Section 3 describes the methods used, from database compilation to modeling the landslides and tsunamis, and the setup. Section 4 describes and interprets the results from the analysis of the database, Section 5 describes and discusses the results from the landslides simulations and Section 6 describes and discusses the results from the related tsunami sensitivity. Conclusions are summarized in Section 7.

2. Geological Setting

The Gulf of Cadiz is located in the SW Iberian Margin (Figure 1). It's seismicity is characterized by continuous shallow to deep earthquakes of low to moderate magnitude of $M_w < 5.5$ (Buforn et al., 1995, 2004; Stich et al., 2005, 2007, 2010). At longer time intervals, this region is also the source of the largest and most destructive earthquakes that have affected Western Europe such as in AD 1531, 1722, 1755, and 1969 (Fukao, 1973). The 1755 Lisbon Earthquake, estimated $M_w > 8.5$, destroyed Lisbon with an intensity of X-XI MSK and was accompanied by tsunamis that devastated the SW Iberian and NW African coasts (Baptista et al., 1998; Baptista & Miranda, 2009). On the basis of geological evidence, geophysical data and tsunami modeling (e.g., Gutscher et al., 2002; Gràcia, Danobeitia, Vergés, & PARSIFAL-Team, 2003; Zitellini et al., 2004, 2009), different faults,

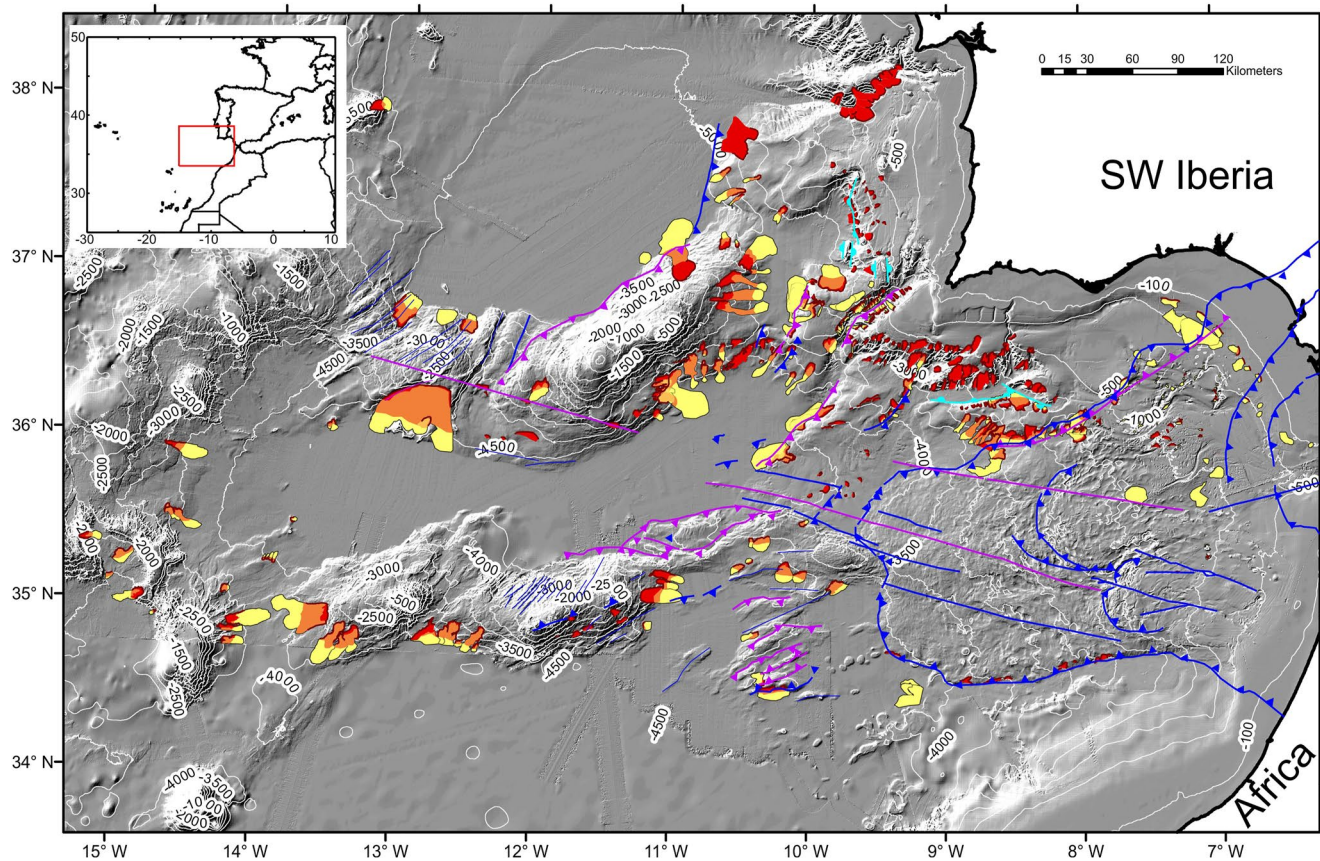


Figure 1. Shaded relief map of the Gulf of Cadiz with depth contours annotated every 500 m displaying the submarine landslides inventory of the Gulf of Cadiz (Dark red color line shows the landslide scars, red polygons show source areas, yellow polygons show deposits, and orange color indicates overlap between source area and deposits). Also shown on the map are the major tectonic features of the Gulf of Cadiz separated according to their activity (purple: active; blue and cyan: inactive). Thrust/reverse faults are shown by purple/blue lines with triangles located on the hanging-wall side of the fault. Normal faults are shown by cyan lines with hemicircles. Strike-slip faults and other tectonic lineaments are shown by simple purple/blue lines.

and mechanisms have been proposed for the source of the Lisbon Earthquake (Gràcia, Danobeitia, Vergés, & PARSIFAL-Team, 2003; Gutscher et al., 2002; Stich et al., 2007; Terrinha et al., 2009; Zitellini et al., 2009, 2004).

Active structures in the Gulf of Cadiz correspond to the NE-SW trending west-verging folds and thrusts of the Marques de Pombal Fault, Horseshoe Fault and Coral Patch Ridge Fault, which are located at the external part of the Gulf (Gràcia, Danobeitia, Vergés, & PARSIFAL-Team, 2003; Terrinha et al., 2009; Zitellini et al., 2004). In addition to these structures, long WNW-ESE dextral strike-slip faults, referred to as SWIM Lineations, have recently been identified (Bartolome et al., 2012; Terrinha et al., 2009; Zitellini et al., 2009). The main active structures are:

1. The Marques de Pombal Fault (MPF): a 50 km long, west verging, monocline thrust cutting through the Plio-Quaternary sequence. This fault and associated landslides have been suggested as a potential source of the 1755 Lisbon Earthquake (e.g., Gràcia, Danobeitia, Vergés, Bartolomé, & Córdoba, 2003; Vizcaino et al., 2006; Zitellini et al., 2004)
2. The Horseshoe Abyssal Thrust (HAT), a 30° dipping thrust separating exhumed mantle in the NW from oceanic lithosphere to the SE (Martínez-Loriente et al., 2014), which is now considered to span from the MPF to the Lineament South (see below) being the most plausible source of the 1755 Lisbon Earthquake (Martínez-Loriente et al., 2021). The HAT has been identified from wide angle seismics modeling (Martínez-Loriente et al., 2014) and suggests the onset of subduction at the external part of the Gulf of Cadiz. Deployment of an Ocean Bottom Seismographs (OBS) network during a year at the external part of the Gulf of Cadiz, shows that earthquakes in the Horseshoe Abyssal Plain are generated in the upper mantle at depths between 40 and 60 km (Geissler et al., 2010; Stich et al., 2010)

3. The deep segment of the Lineament South: a seismogenic WNW-ESE trending, 3–6 km wide dextral strike-slip fault (Bartolome et al., 2012). The fault trace is associated with deep-water (>4 km) mud volcanoes, evidence of rising deep fluids, and formation of gas hydrates along the fault (Hensen et al., 2015)

The recurrence rate of great magnitude ($M_w > 8$) Holocene earthquakes has been investigated in the Gulf of Cadiz using “turbidite paleoseismology” on the basis of widespread synchronous turbidite deposits in the Tagus and Horseshoe Abyssal Plains (Garcia-Orellana et al., 2006; Gràcia et al., 2010). These deposits have been correlated to tsunami deposits on-land (Lario et al., 2010) yielding a regional recurrence interval of $M_w > 8$ earthquakes of about 1,800–2000 years (Gràcia et al., 2010).

Submarine landslides are ubiquitous in the Gulf of Cadiz (Gamboa et al., 2021; Urgeles & Camerlenghi, 2013). Some of the largest landslides include the North Gorringe Bank debris avalanche, which released a volume of 80 km³ (Lo Iacono et al., 2012) and the South Hirondelle Slide with a volume of 500 km³ (Omira et al., 2016). Numerical tsunami simulations indicate that both landslides are potentially tsunamigenic, causing a tsunami with surface elevations of 7 m at some locations along the NE Atlantic coasts (Omira et al., 2016) and up to 20 m in Sines, Portugal (Lo Iacono et al., 2012). Submarine landslides, such as the Marques de Pombal slide (Vizcaino et al., 2006) and the North Gorringe debris avalanche (Lo Iacono et al., 2012), are often associated with active faults and likely to be seismically triggered.

The Late Pleistocene sea level in the Gulf of Cadiz is characterized by high amplitude and low frequency, approximately every 100 kyrs, oscillations coinciding with glacial-interglacial cycles, while the Early Pleistocene shows lower amplitude but higher frequency oscillations (Rodero et al., 1999). The sea-level fall during the last glacial maximum, from 26.5 to 19 ka, reached 130 m below the present-day level (Clark et al., 2009), while prior late Quaternary sea-level lowstands remained mostly above depths of 110 m (Posamentier, 2001). In the Late Quaternary, sea level in the Iberian margin of the Gulf of Cadiz has also been controlled by tectonic processes mostly due to the relative motions between Iberia and Africa. This translated in a series of relative sea level falls in between 295 and 135 ka with the highstands in between the falls located at 65–70 m below present sea level (Rodero et al., 1999).

3. Methods

3.1. Landslide Database Compilation

Run-out distances from the submarine landslide database are used to constrain input parameters in landslide modeling, which helps to limit epistemic uncertainties related to landslide material parameters. The database used in this study currently contains 471 events that have been mapped using geomorphological criteria on multibeam bathymetric data, and using seismic/acoustic facies in sub-bottom and Multi-Channel Seismic (MCS) profiles. The data are supplemented with information digitized/obtained from the scientific literature. This database represents a significant step forward with respect to previous submarine landslide databases for the Gulf of Cadiz, which were based exclusively on published information (see Urgeles and Camerlenghi (2013) and references cited therein). The number of events mapped by Urgeles and Camerlenghi (2013) for the Gulf of Cadiz was 77.

The swath-bathymetric data used in this study is a compilation of measurements acquired using different multibeam echosounder systems during a total of 20 marine cruises that were carried out between 2001 and 2009 and known as the SWIM compilation (Zitellini et al., 2009). The SWIM bathymetric grid has a node spacing of 100 m.

MCS and sub-bottom profiler data used for this study were acquired with different configurations during multiple marine surveys: (a) the ARRIFANO survey with the R/V OGS EXPLORA in 1992 (acquisition data and processing parameters reported by Zitellini et al. (1999) and Zitellini et al. (2009)); (b) the IAM cruise in 1993 aboard M/VGeco Sigma (Banda et al., 1995); (c) the BIGSETS survey carried out in 1998 onboard the R/V URANIA (Zitellini et al., 2001, 2004); (d) the PD00 survey acquired by TGS-NOPEC in 2000 (Brackenridge et al., 2013; Llave et al., 2011); (e) the 2001 SISMAR cruise onboard the R/V Le Nadir (Gutscher et al., 2002); (f) the 2002 VOLTAIRE survey onboard the R/V URANIA (Terrinha et al., 2009); (g) the SWIM 2006 cruise onboard the R/V Hesperides (Bartolome et al., 2012); and (h) the INSIGHT Leg 1 (2018) and Leg 2 (2019) cruises, carried out with the R/V Sarmiento de Gamboa (Ford et al., 2020). Interpretation of the network of MCS profiles has been carried out using the “IHS Kingdom Suite” seismic interpretation software. Time-to-depth conversion is

used to determine the thickness of deposits and assumes a constant water velocity and a linear velocity gradient with depth below the seafloor calibrated with IODP Expedition 339 borehole sonic data (Stow et al., 2013). The water velocity was set to $1,514 \text{ m s}^{-1}$ and the sediment velocity gradient was 491 m s^{-2} (see also Mencaroni et al., 2020).

The extent of the landslide source area in the database is used to determine a mean source slope angle using zonal statistics in ArcGIS, and to extract the source area width and length. The length is measured from the deepest to shallowest cell inside the source polygon and the width is measured perpendicular to it. The source volume is calculated by multiplying the source area with the mean headscarp height, which is measured from bathymetric and/or seismic data. If the mean headscarp height cannot be properly determined, for example, buried landslides with limited seismic data coverage, then the source volume is calculated based on a source volume-area power-law relationship (Figure 2a). The source volume-area power-law relationship is obtained for landslides in the database in which both area and mean headwall scarp could be measured.

The deposit volume is calculated by multiplying the deposit area with the mean deposit thickness. This thickness is either estimated from (a) seismic/subbottom profiler data, (b) elevation profiles across the width of the deposit or (c), in case where only the deposit area is available but not the mean deposit height, for example, for some bibliographic data, then the volume is calculated based on the deposit volume-area power law. A power-law fit between source volume and deposit volume results in an exponent with value 1.0931 where the value 1 indicates the equal source and deposit volume. As the landslide volume estimates from the sources are similar to the ones from the deposits, we use the information from both the source and deposit volume for further analyses on the run-out ratio versus volume. Therefore, if both source and deposit volumes are available for a specific landslide, we take the mean value. If either the source volume or the deposit volume are available, we take the volume that is available.

Fitting power laws to the size (volume) distribution of submarine landslides in the Gulf of Cadiz was accomplished following the method detailed in Clauset et al. (2009) using the R software (R-Core-Team, 2012) and the `powerLaw` package (Gillespie, 2014). For power fits of bivariate data (e.g., volume-area relationship in Figure 3), the empirical data were log transformed and a maximum likelihood (Tukey bisquare) robust linear fit (Venables & Ripley, 2010) was used to account for problems associated with outliers and the fitting of data spanning multiple orders of magnitude.

3.2. Landslide Dynamics Model

The cohesive landslide model BingClaw is used to simulate the landslide dynamics. BingClaw incorporates a depth-averaged Herschel-Bulkley rheology for the landslide motion in two horizontal dimensions in two-layer formulation (Kim et al., 2019; Løvholt et al., 2017; Vanneste et al., 2019), where the top layer represents a plug flow where no shear deformation takes place, and a bottom-layer subject to shear deformation. External hydrodynamic resistance forces acting on the landslide from the ambient water are also included in BingClaw through pressure and frictional drag terms that are both proportional to the square of the landslide velocity, and the added mass. Corresponding coefficients to each of these force terms are C_p , C_f , and C_m , respectively.

The model takes into account yield strength remolding of the entire landslide mass using an ad-hoc parameterization proposed by De Blasio et al. (2005) mimicking soil-softening behavior with increasing shear deformation.

$$\tau_y(\gamma) = \tau_{y_r} + (\tau_{y_0} - \tau_{y_r}) e^{-\Gamma\gamma} \quad (1)$$

where τ_{y_r} is the residual yield strength, τ_{y_0} the initial yield strength, Γ the remolding rate, and γ the accumulated shear deformation. Additional material properties are described using the material exponent n and the maximum strain rate $\dot{\gamma}_r$, and the mass density ρ_s . The reference strain rate $\dot{\gamma}_r$ relates dynamic viscosity, yield strength and the Herschel-Bulkley flow exponent. For more details related to the BingClaw model, see Kim et al. (2019). In this paper, BingClaw is used for two purposes. The first purpose is to simulate the landslide run-out distance that is used for comparing simulations with observed landslide statistics. The second purpose is to use the time dependent landslide shape as a source term in the tsunami simulations. The landslide simulations used for the tsunami source modeling are more resource intensive because their outputs needs to be more densely sampled,

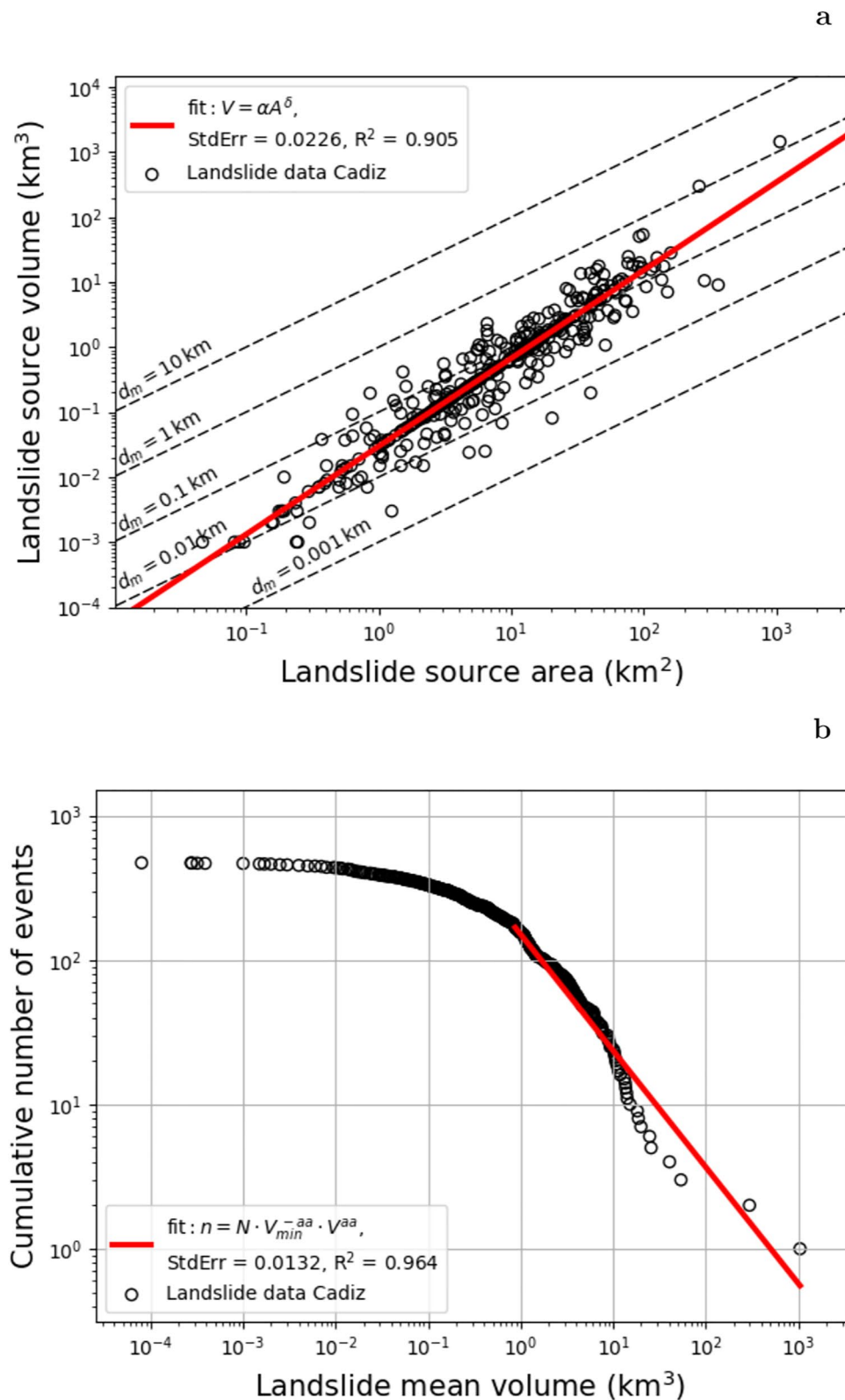


Figure 2. (a) Landslide source volume versus source area graph for submarine landslides in the Gulf of Cadiz. Values for α and δ for the fitted power law are 0.0298 km and 1.36, respectively. The dashed parallel lines highlight theoretical area-volume relationships for landslides with constant mean source area thicknesses. (b) Cumulative-volume distribution with a power-law behavior for landslides larger than the estimated rollover $V_{\min} = 0.874 \text{ km}^3$ using the package powerLaw in R-statistics. The power-law exponent is $aa = -0.806$, $N = 168$ is the number of events larger than V_{\min} , and n is the cumulative number of events.

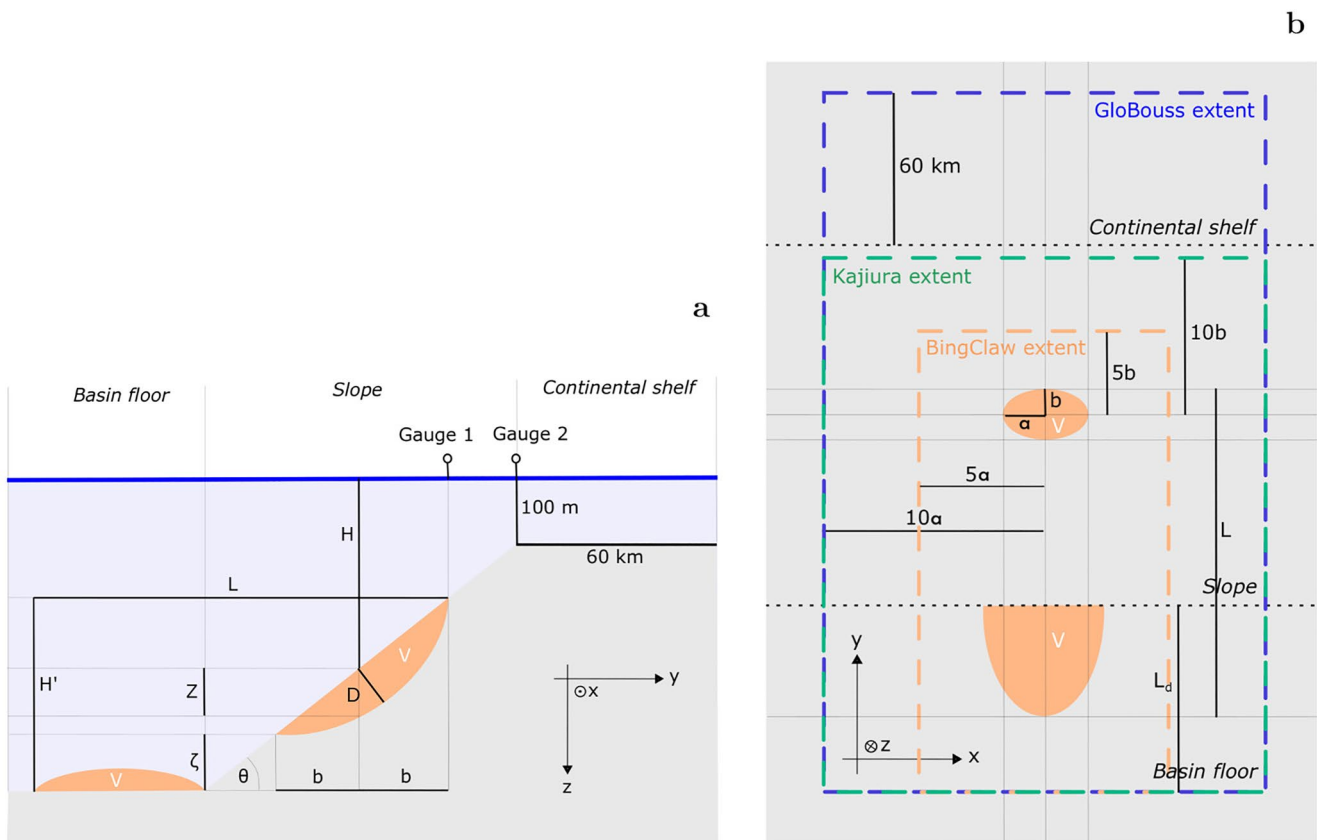


Figure 3. Principle sketch (a) side view with the slope parameters used in this study and (b) top view of the model grid extents. The landslide volume V is shown prior to failure and after motion at rest in orange color. The investigated slope parameter ranges of the shown quantities are listed in Table 1. In panel b we see how the extents of the landslide simulations BingClaw, the Kajiura filtering domain, and the tsunami simulation domains differ.

and they are therefore carried out independently from the simulations used for comparing with the observed run-out distances.

3.3. Tsunami Model

We use the depth-averaged dispersive long-wave model GloBouss to simulate tsunami generation and the tsunami propagation due to the submarine landslide over varying bathymetry (Løvholm et al., 2008, 2010; Pedersen & Løvholm, 2008). We note that while the full GloBouss model contains a first order Boussinesq approximation with optimized dispersion, we only use the linear dispersive equation set here as non-linearities play a negligible role in the tsunami generation that takes place in relatively deep water (at more than 100 m water depth). The primary source of the tsunami generation is the volume displacement of the landslide. This time dependent volume displacement enters as volume flux terms in GloBouss (Løvholm et al., 2015), that is, as functions of the differential seafloor-displacement to time-step ratio. The wave generation is affected by the hydrodynamic response due to the volumetric water displacement from the landslide. To take this effect into account, a simplified model that conveys the vertical seabed displacements induced to by the landslide into vertical sea surface displacements is used. This model is based on full potential wave theory and assumes for each local grid cell that the depth is constant (Kajiura, 1963; Løvholm et al., 2015). The wave generation model is applied each time a new landslide displacement file is fed into the GloBouss model. As this is the most computationally expensive step in the analysis, the source output time stepping is optimized for computational efficiency. See Zengaffinen-Morris (2021) for more details.

3.4. Model Setup

In this study, we investigate the adverse effect of different parameters on landslide run-out and tsunami-generation. To discriminate between, parameters related to material and hydrodynamic resistance forces, and water depth and slope, we adopt the following nomenclature: The term *landslide parameter* is as an overarching definition for all model input parameters related to the landslide. Then the term a *landslide material parameter* is used for both material parameter of the landslide and the hydrodynamic resistance force parameters acting on the landslide, while the term *slope parameter* describes the source geometry of the slope including the initial landslide volume and water depth of tsunami generation.

3.4.1. Model Geometry and Slope Parameters

A simplified bathymetric and source representation was chosen in order to provide a transparent model setup and analysis. Use of the actual bathymetry of the Gulf of Cadiz would render the wave analysis more site dependent, and the analysis of the tsunami-generation would consequently be less transparent. Hence, we chose to represent the bathymetry through an inclined plane with a slope angle θ separating two horizontal planes. We employ a Cartesian coordinate system (Figure 3). The shallowest horizontal plane is extended 60 km shorewards, having a constant depth of 100 m for all simulations. Down-slope there is a flat basin floor whose water depth depends on the simulation purpose.

The initial landslide volume is shaped as an elliptical paraboloid that is defined as

$$\xi = \frac{(x - x_c)^2}{a^2} + \frac{(y - y_c)^2}{b^2} \quad (2)$$

where x , y , and ξ represent a separate orthogonal coordinate system to that defined in Figure 3 in the simplified geometric setup. The only difference is that the ξ -axis' points in the opposite direction to the z -axis. The elliptical paraboloid can be divided into multiple horizontal ellipses, with the base ellipse being the largest ellipse. The base ellipse is at $\xi = 0$ whose area equals $A(0) = \pi ab$. The area of any ellipse perpendicular to the vertical ξ -axis is given by:

$$A(\xi) = \pi ab \left(1 - \frac{\xi}{D}\right) \quad (3)$$

where a is the radius of the base ellipse in the x -direction (alongshore), and b the radius of the base ellipse in the y -direction (cross-shore). The center of these horizontal ellipses are all located at the coordinates x_c and y_c . D is the maximum thickness of the elliptical paraboloid, hence, also the maximum initial landslide thickness. The landslide volume is given by:

$$V = \int_0^D A(\xi) d\xi = \frac{1}{2} \pi a b D = \frac{1}{2} A(0) D. \quad (4)$$

In Section 5.3, we vary the shape factors a and b to investigate model sensitivity. In order to also systematically vary the initial maximum landslide thickness D and keeping the volume constant, we introduce a thickness factor d_F . The modeled landslide thickness is then $D = d_F D'$, where D' is the mean thickness based on the landslide database (see Section 4). Equation 4 for the landslide volume transforms then into:

$$V = \frac{1}{2} A(0) d_F D', \quad (5)$$

which enables us to model different landslide configuration realizations spanning from deep-seated to thinly shaped landslides. We remark that the area of the base ellipse is reduced when the thickness factor d_F is increased to keep the volume constant, while keeping the same aspect ratio ab .

This landslide volume is subtracted from the bathymetry at a desired location on the constantly inclined slope to construct the initial failure plane for individual synthetic submarine landslide scenarios. The viscoplastic material

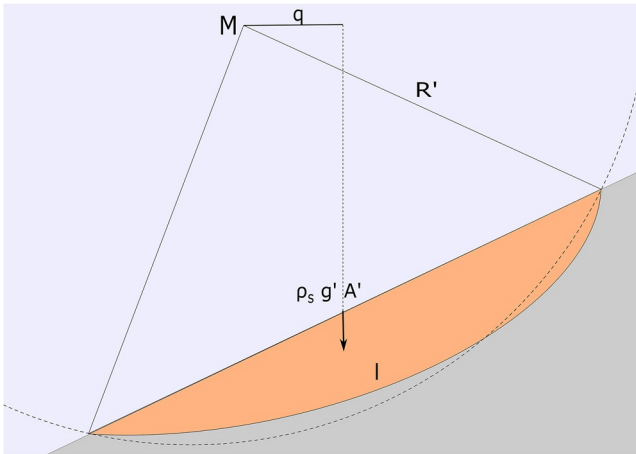


Figure 4. Factor of safety calculation in terms of total stress. We use the factor of safety, together with other slope parameters, to estimate the initial yield strength of the landslide material. The gray area represents the stable slope, the orange area the landslide mass, and the purple area represents seawater.

then fills this excavated volume such that its upper surface is continuous with the surrounding slope. If the initial setup of the landslide allows materials to cut the continental shelf (Figure 3), then this landslide parameter constellation is removed from the selection.

Two different sets of landslide batch simulations are carried out. The first batch contains the most elaborate sensitivity analysis equaling a total of 4,374 simulations related to the statistical description of landslide run-out distance, comparing simulations with the statistical variability in the Gulf of Cadiz. This analysis is presented in Section 5. For these landslide run-out simulations the water depth of the basin floor was fixed to a water depth similar to the deepest part of the Gulf of Cadiz at 4,200 m. For the coupled landslide-tsunami analysis presented in Section 6, a second batch consisting of a smaller set of simulations were carried out (a total of 3,645), as these simulations required more comprehensive computational resources. In order to tailor the landslide simulations to the needs in the tsunami sensitivity study, we varied the terminal depth of the (deep) basin floor for investigating the effect of the free parameter ζ on the tsunami-generation. Independent tests verified that varying the basin floor depth did not have significant influence on the tsunami-generation, as most of the tsunami generation takes place in the initial stages of the landslide motion.

3.4.2. Scaling the Landslide Material Parameters

Main landslide material parameters describing the soil in BingClaw comprise the residual yield strength τ_{y_r} , the initial strength τ_{y_0} , and the soil sensitivity $f = \frac{\tau_{y_0}}{\tau_{y_r}}$. We scale the initial yield strength τ_{y_0} based on a simple factor of safety F consideration (see derivation below). This is done in order to normalize the yield strength based on the thickness and shape of the initial failure.

Figure 4 illustrates the simplified factor of safety calculation in terms of total stress. We consider a cross-section through the center of the initial landslide mass parallel to the y -axis. The curvature of the failure surface is approximated by a circular shape, which results in a virtual circle center M . The factor of safety is:

$$F = \frac{\text{resisting momentum}}{\text{driving momentum}} = \frac{R' \tau_{y_0} l}{\rho_s g' A' q} \quad (6)$$

where $g' = g \left(1 - \frac{\rho_w}{\rho_s}\right)$ is the reduced gravitational acceleration, R' the radius from M to the approximated circular failure surface in the cross-section, l the arc length of the approximated failure surface, A' the cross-sectional area of the landslide mass, and q the horizontal distance between M and the landslide's initial mid position on the slope. The slope angle θ increases with increasing q . Reformulating Equation 6 leads to the initial yield stress:

$$\tau_{y_0} = \frac{\rho_s g' A' q F}{R' l}. \quad (7)$$

As the landslide simulations involve remolded material after failure, we set the factors of safety to less than unity, and investigate low values of F , including 0.05, 0.35, and 0.65 (see Table 1), following also similar arguments to those of Sawyer et al. (2012).

Scaling τ_{y_0} with the factor of safety, and scaling τ_{y_r} with τ_{y_0} and f , restricts a thin landslide from being too stiff, and a thick landslide from being too soft. It also results in material parameter ranges for τ_{y_0} and τ_{y_r} , which makes these values more physically reasonable considering the large variety of initial landslide thicknesses in this study.

Table 1
Model Input Parameter Values

Fixed parameter	Symbol	Values	Unit
Herschel-Bulkley flow exponent	n	0.5	–
Reference strain rate	$\dot{\gamma}_r$	1000	s ⁻¹
Landslide density	ρ_s	2000	kg/m ⁻³
Sea water density	ρ_w	1000	kg/m ⁻³
Gravitational acceleration	g	9.81	m s ⁻²
Landslide material parameter	Symbol	Values	Unit
Factor of safety	F	0.05, 0.35, 0.65	–
Soil sensitivity	f	2, 5 , 8	–
Remolding coefficient	Γ	0.0005, 0.005 , 0.05	–
Hydrodynamic friction drag coefficient	C_F	0.001, 0.01 , 0.1	–
Hydrodynamic pressure drag coefficient	C_P	0.1, 1.0 , 10.0	–
Added-mass coefficient	C_m	0.01, 0.1 , 1.0	–
Slope parameter	Symbol	Values	Unit
Slope angle	θ	3.02, 5.96 , 11.77	°
Landslide thickness factor	d_F	0.316, 1.0 , 3.16	–
Landslide source area width to length ratio	$\frac{a}{b}$	0.47, 1.04 , 2.33	–
Vertical distance from the initial Landslide toe to the basin floor	ζ	0 , 750, 1,500	m
Initial landslide center water depth	H^a	1,000, 2,000, 3,000	m
Landslide volume	V	0.04, 0.2, 1, 5, 25, 125 ^b	km ³

Note. Values in bold are used for the example landslide model runs presented in Section 5.1 and for the results in Figure 12 if not investigated.

^aOnly applied for the coupled landslide-tsunami simulations to investigate the tsunami uncertainty. ^bOnly applied for the landslide run-out fitting.

4. Landslide Characteristics in the Gulf of Cadiz

From the 471 events in the landslide database, 193 contain information on both deposit and source area, 182 contain information on source area only, and 96 on deposit area only. In terms of magnitude indicators, the database includes landslides whose source area ranges from $3 \cdot 10^{-2}$ to 10^4 km². The source volumes ranges from $3 \cdot 10^{-4}$ to 10^3 km³. A power-law relationship can be fitted to the source volume-area data for landslides in the database. According to Figure 2a, the power-law exponent for this relationship is $\delta = 1.36$, which implies that the failed thickness grows with the source area affected. With regard to the sediment pile that is involved by these landslide events, its thickness may range from a few meters to slightly more than 1 km, but only a few landslides involve sedimentary sequences of more than 200 m (Figure 2a).

Figure 2b shows a cumulative-volume distribution based on the mean volume for all mapped landslides in the Gulf of Cadiz. A power law can be fitted to the landslide volumes larger than $V_{min} = 0.874$ km³. We infer that the power law can actually be extended in the range of landslides smaller than the minimum volume fitted, as there is likely a lack of mapped smaller events (Urgeles & Camerlenghi, 2013).

Landslides in the Gulf of Cadiz are found in almost all mean water depths (mwd) from 150 to nearly 5,000 mwd. Most landslides originate, however, from the 800 to 2,200 mwd depth range. They occur on slopes ranging from almost zero to $\theta = 21.9^\circ$ following a lognormal distribution. The probability density function for a lognormal distribution is given by

$$P(j) = \frac{1}{\sigma \sqrt{2\pi} j} e^{-\frac{(\ln j - \mu)^2}{2\sigma^2}} \quad (8)$$

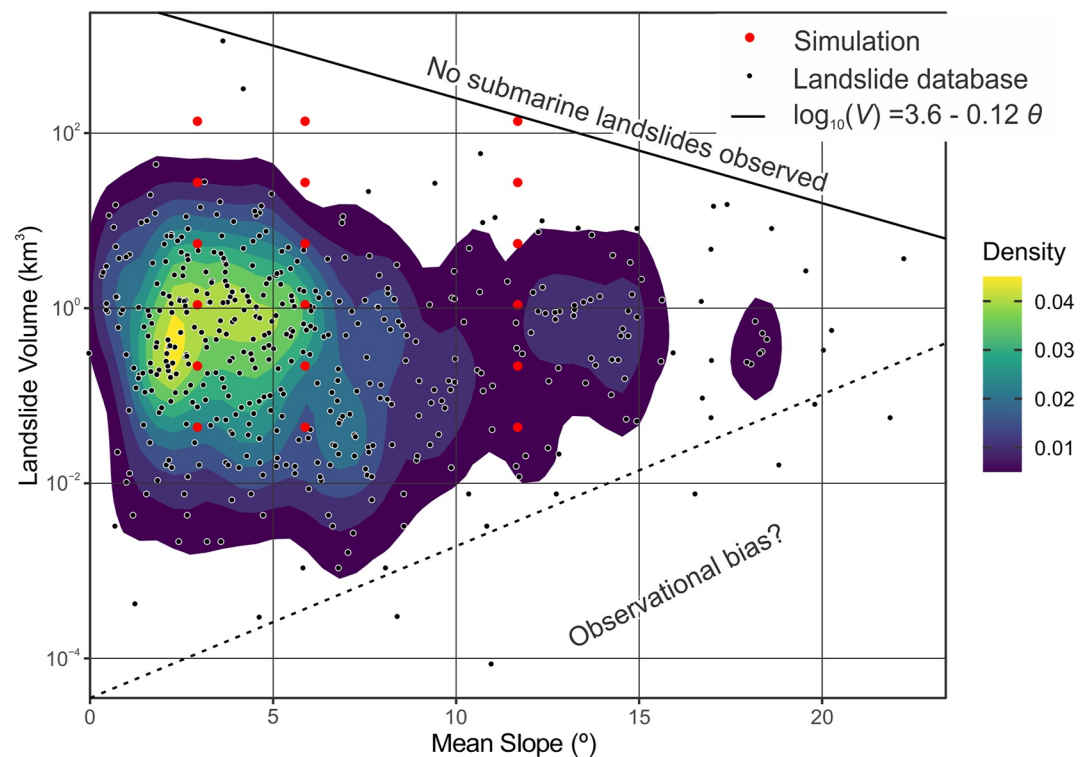


Figure 5. Mapped submarine landslide volumes from the database versus slope angle at the source (including kernel density contours) together with simulation setup. The cut-off function, $\log_{10} V = 3.6 - 0.12 \cdot \theta$, indicates that landslides above this line, meaning large landslides on steep slopes, are not observed. All simulated landslides investigated are below this line.

where j is the investigated parameter, here θ , μ a location parameter, and σ a shape parameter with $GM = e^\mu$ the geometric mean, equal to the median in the lognormal distribution, and $GSD = e^\sigma$ the geometric standard deviation. A majority of the landslides occur in the slope range from $GM/GSD = 3.02^\circ$ to $GM \cdot GSD = 11.77^\circ$ with $GM = 5.96^\circ$. It should be noted that the range of slopes from 3.02° to 7° is the most abundant in the area and that slopes higher than 7° are restricted to limited areas such as canyon and diapir flanks as well as fault scarps.

When it comes to the magnitude distribution of submarine landslides with respect to slope angles, we find that not all slopes can host all landslides. A cut-off function, $\log_{10} V = 12.6 - 0.12 \cdot \theta$, where the landslide volume V is in m^3 and the slope angle θ in degrees, defines the largest volume that a slope of specific gradient can host (Figure 5). Such a relationship, indicating that gentler slopes can host landslides of any size and steeper slopes can only host small landslides, results from the fact that steeper slopes are in general intricate, with the presence of numerous gullies, and therefore compartmentalize stratal surfaces and potential weak layers.

We characterize the landslide source area shape using the width to length ratios, with the length referred to the down-slope axis of the landslide. We find no preferential orientation in landslide source areas indicating equally occurring down-slope and along-slope oriented source areas. Nevertheless, the width to length ratio ranges in between 1:12 and 15:1 following a lognormal distribution. Most landslides concentrate between $GM/GSD = 0.47$ and $GM \cdot GSD = 2.33$ with $GM = 1.04$.

The run-out ratio H'/L , which is the tangent of the angle of the line connecting the highest point of the landslide scarp to the distal margin of the displaced mass, has been considered as a measure of the relative mobility of a landslide (see Hungr et al., 2005 and references therein). The field within the dashed line in Figure 6 represents the extent in the $H'/L-V$ space for submarine landslides reported by De Blasio et al. (2006). This field shows a decreasing run-out ratio with increasing volume. According to Figure 6, we find considerable scatter in the H'/L ratio for all volume sizes in the Gulf of Cadiz if the slope angle at the source is not considered. It only shows a marginal trend displaying decreasing run-out ratio with increasing landslide volume. However, we find a strong

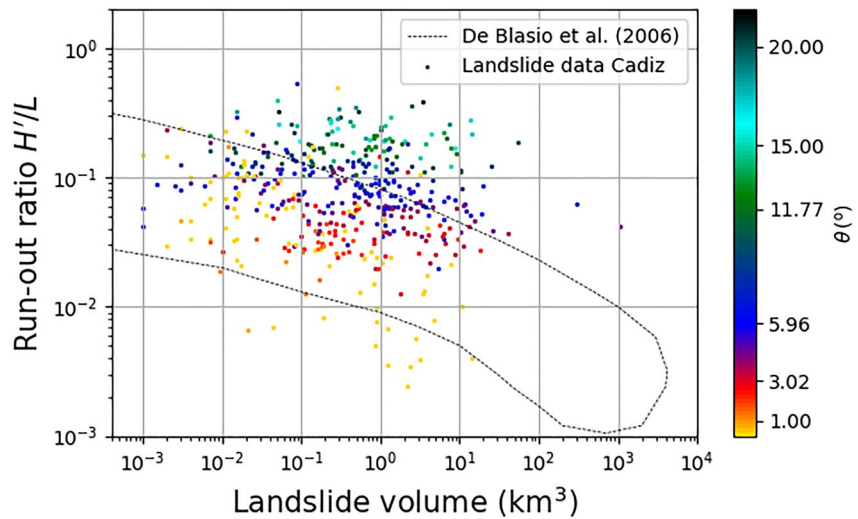


Figure 6. Run-out ratio versus landslide volume for the Gulf of Cadiz submarine landslide database. The slope angle at the source, θ , is color-coded. The field marked with dashed line represents the scatter in H'/L versus volume for submarine landslides from De Blasio et al. (2006).

dependency of the run-out ratio with the slope angle at the source of the landslide. Figure 6 indicates that the run-out ratio displays a consistent decrease with increasing volume within a specific slope angle at the source.

Previous studies suggest that submarine landslides have an order of magnitude lower run-out ratios than their subaerial counterparts of similar volume (De Blasio et al., 2006; Hampton et al., 2002; Locat & Lee, 2002). It is possible that the initial slopes from which the field of subaerial and submarine landslides were originally defined, included subaerial landslides on relatively steep slopes and submarine landslides on gentle slopes. This is likely a result of the slope gradients where landslides are typically mapped in these environments, implying that the smaller landslides that typically occur on steeper slopes have received little attention. We find submarine landslides that typically fall in the field previously defined for submarine events, but many of the submarine landslides in the Gulf of Cadiz are also present in the field that was previously designated for subaerial events, in other words with higher H'/L ratios compared to the field drawn by De Blasio et al. (2006) in Figure 6. The main reason for this is likely that, unlike previous studies, our database includes relatively small submarine landslides in steep canyon walls and fault scarps.

From the results in Figure 6, we postulate that there is no actual separation in between subaerial and submarine landslides in the H'/L ratio versus landslide volume plot. Nevertheless, we remark that submarine landslides can have extremely large run-out distances on low slope angles, which does not occur for subaerial landslides due to differences in the properties of the respective ambient fluids. An additional conclusion from Figure 6 is that landslides in the steepest terrain are those producing the largest run-out ratios (H'/L) and therefore lower relative run-out distance, which links the initial static angle of resistance or shear strength to the rheology of the landslide mass.

5. Landslide Run-Out Simulations and Comparison With Observations

5.1. Examples of Landslide Kinematics From Single Model Runs

Here, we consider a simulation with the following fixed landslide parameters, $alb = 1.04$, $d_f = 1.04$, $\zeta = 0$ m, and $\theta = 5.96^\circ$, $F = 0.65$, $f = 5$, $\Gamma = 0.005$, $C_F = 0.01$, $C_p = 1.0$, and $C_m = 0.1$ (see bold values in Table 1). For tests on model convergence on grid resolutions as well as on the effect of the finite duration of the landslide motion on the tsunami-generation, we refer to Zengaffinen-Morris (2021).

In the first example, we set $V = 25$ km³. Figure 7 shows the initial landslide configuration, and the slide thickness at 210, and 510 s after landslide initiation, and at 800 s when the landslide motion has stopped. Most parts of

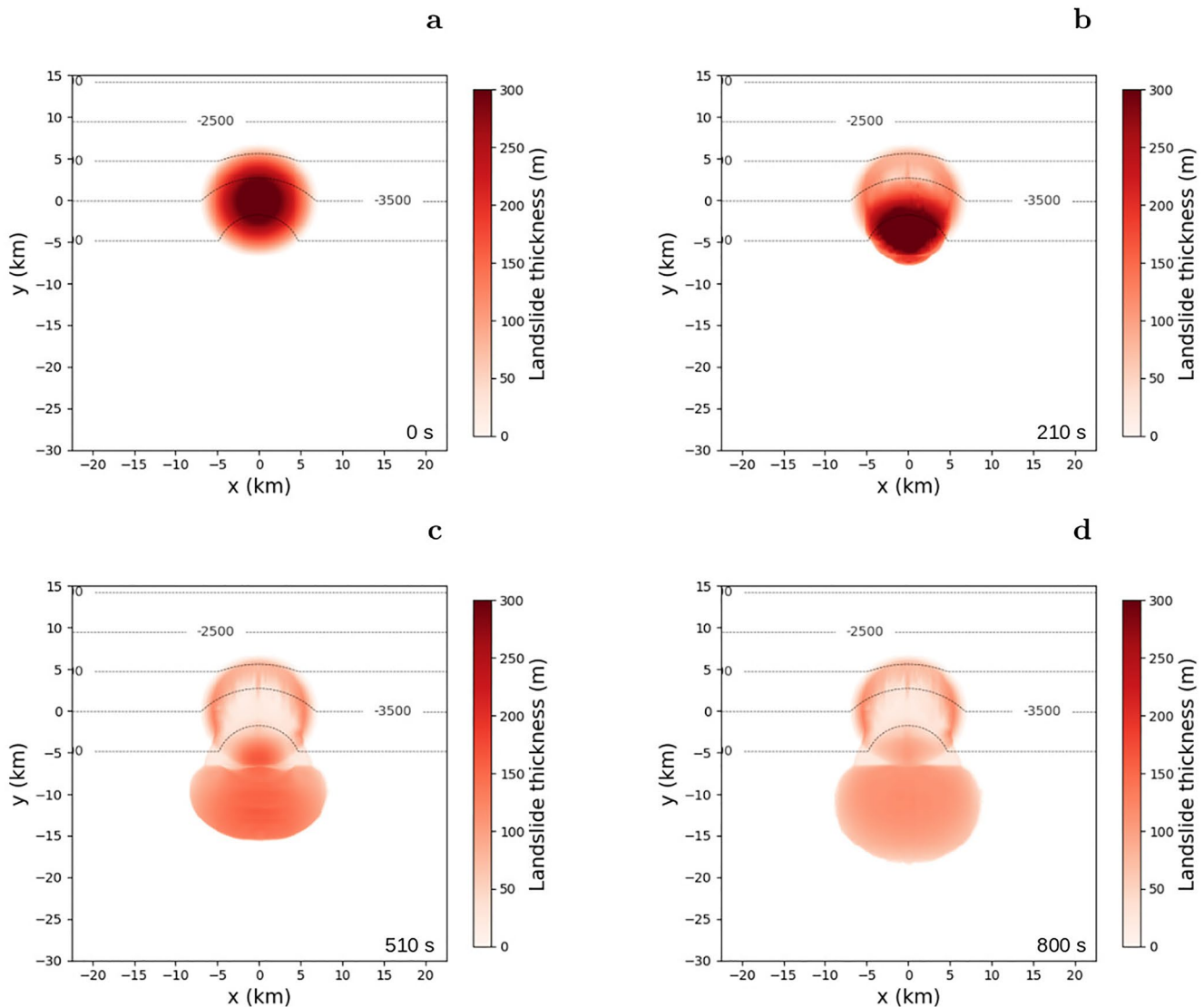


Figure 7. Top view of simulated landslide (a) prior to the release, (b) 210 s, (c) 510 s after initiation, and (d) at 800 s when the motion has stopped. Landslide parameters are $V = 25 \text{ km}^3$, $d_F = 1.0$, $\zeta = 0 \text{ m}$, $\theta = 5.96^\circ$, $a/b = 1.04$, $F = 0.65$, $f = 5$, $\Gamma = 0.005$, $C_F = 0.01$, $C_P = 1.0$, and $C_m = 0.1$.

the landslide mass flow out of its source area after 300 s, and run out on the constant depth basin floor. A small portion of the mass remains at the source area.

Figures 8a and 8b shows maximum and mean landslide velocities from simulation results for various landslide volumes, using the same landslide parameter values as the example shown in Figure 7. We define the maximum velocity as the maximum over the entire spatial domain for each computational time step, and the mean velocity as the average over the entire spatial domain for each computational time step. The maximum and mean accelerations shown in the same figure are defined in the same way as the velocities. The peak maximum and peak mean velocity is the largest value of the corresponding quantity for all times. Figures 8a and 8b show that the more voluminous landslides provide larger velocities, while the velocity peaks are delayed in time with increasing volume. A secondary peak is observed for the maximum value but this does not appear for the mean velocity. This delayed peak occurs due to a late failure involving a small portion of the mass mobilized later than the main part of the landslide, which is due to the material remolding. When using the analysis in correlation studies with the tsunami-genesis below, we use the peak mean velocities as it is considered the most stable measure. Related landslide accelerations follow the same pattern as the velocities, with larger accelerations for the larger landslide

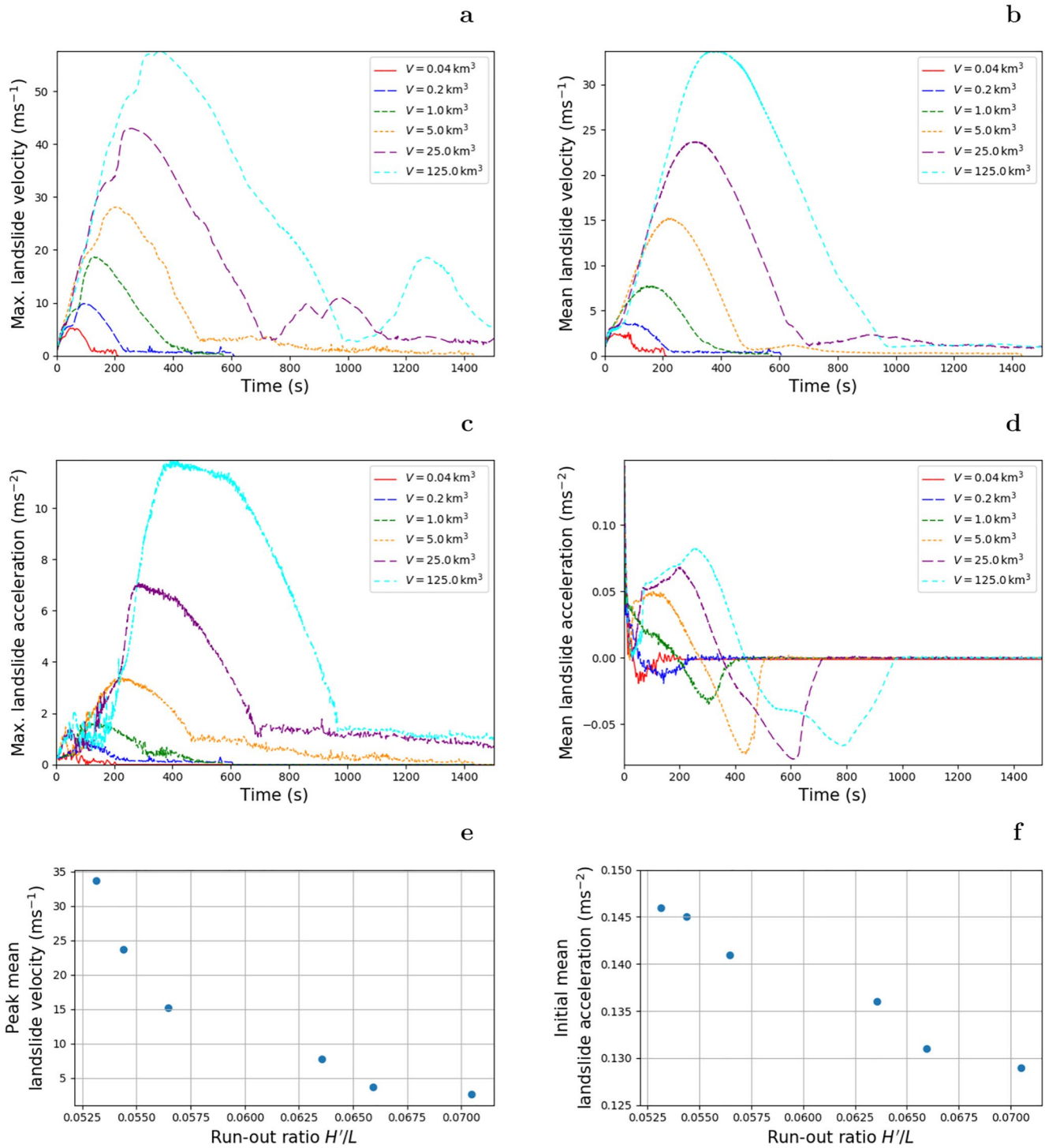


Figure 8. (a) Maximum and (b) mean velocity time evolution, (c) maximum and (d) mean acceleration time evolution, and (e) peak mean velocity and (f) initial mean acceleration versus run-out ratio. Landslide parameters are $d_F = 1.0$, $\zeta = 0 \text{ m}$, $\theta = 5.96^\circ$, $a/b = 1.04$, $F = 0.65$ that governs τ_{y0} , $f = 5$ that governs τ_y , $\Gamma = 0.005$, $C_F = 0.01$, $C_P = 1.0$, and $C_m = 0.1$. Increasing peak mean velocities decrease the run-out ratio, therefore induce a relative increase in the run-out distance.

volumes, as shown in Figures 8c and 8d. However, the initial mean acceleration values are less sensitive to the volume.

Figures 8e and 8f shows the relationship between the run-out ratio and the peak mean landslide velocity and initial mean landslide acceleration, respectively. The run-out ratio decreases with both increasing peak mean landslide velocity and increasing initial mean landslide acceleration. This pattern can be straightforwardly explained by the fact that the landslides with higher velocity and acceleration are more mobile (i.e., having lower H'/L ratios) as expected. The peak mean velocities and initial mean accelerations are hence good proxies for the run-out ratio in these examples. This should be recalled in the broader parametric sensitivity analysis below.

5.2. Input Landslide Parameter Values for the Sensitivity Study

Below, we carry out a set of different sensitivity studies aimed to investigate the effect of a subset of the landslide parameters on (a) the run-out ratio H'/L and (b) the landslide kinematics (that influences tsunami-generation). In particular, we are interested in investigating how various combinations of these parameters can help explaining the large span in run-out ratios found in the Gulf of Cadiz. The landslide parameters we have investigated include initial yield strength, the remoulded yield strength, the remolding rate, the hydrodynamic pressure drag coefficient, the hydrodynamic friction drag coefficient, the added-mass coefficient, the aspect ratio of the landslide, the thickness factor, the slope angle, the depth of initial slope failure, the vertical distance between the initial landslide toe to the basin floor, and the landslide volume. As this resulted in an exhaustive set of results, we display a selection of the findings below. First, we briefly discuss sensitivities to individual landslide parameters, varying one parameter while fixing all others. The simulated run-out ratios are shown in Figure 10, while the simulated peak mean velocities are shown in Figure 11. Second, we show the variability taking into account all landslide parameter combinations in Figure 12.

For the parametric sensitivity study, we employ the landslide parameters listed in Table 1. To make the study computationally feasible, we could only resolve the values into a few realizations, and some of these parameters were even fixed to a single value (e.g., density). The investigated range of slope angles cover the majority of landslides events that have taken place in the Gulf of Cadiz as documented in the database. Further, we note that the source width-to-length ratios $a/b = 0.47, 1.04, 2.33$, also cover most of the aspect ratios observed in the database. The values for the elevation ζ measuring the vertical distance from the initial landslide toe to the basin floor are set to 0, 750, and 1,500 m.

The fitted power law in Figure 2a relates the landslide volume to the landslide area through a mean reference thickness D' . However, there is a significant variability in the data, which suggests that the thickness D can be half an order of magnitude smaller or larger than the reference thickness D' for a given volume. Therefore, we apply, $d_F = 10^{-0.5}, 1.0, 10^{0.5} = (0.316, 1.0, 3.16)$, which allows for modeling both thin, intermediate, and deep-seated failures. The latter may also mimic rotational slumps when run-out distances are short. These landslides differ in the initial maximum landslide thickness D , initial failure surface area $A(0)$, and in the curvature of the landslide failure plane.

The landslide mass density is based on borehole data from the International Ocean Discovery Program (IODP) Site U1389 in the Gulf of Cadiz. We fit a power law to the density versus depth and integrate the density over the sedimentary column to obtain a mean density to the mean depth. We approximate each landslide with a mean density of $2,000 \text{ kg m}^{-3}$ as the density fit becomes asymptotic to this value 50 m below the seabed. We employ a Herschel-Bulkley flow exponent $n = 0.5$, and note that Zengaffinen, Løvholt, Pedersen, and Harbitz (2020) found that the tsunami generation is not sensitive to n .

Each of the sensitivity studies is carried out for a range of landslide volumes. These landslide volumes vary from 0.04 to 125 km^3 , where the largest volume corresponds to one of the largest landslides in the database. It should be noted that the modeled landslide volumes are limited by the data window relating slopes and volumes in Figure 5.

The three values for θ , d_F , a/b , and F , and the six values for V , imply $3^4 \cdot 6 \cdot 14 = 450$ possible initial yield strengths. The excluded 14 values result from landslides that are located shallower than 100 m. Those 450 events span a relatively wide range for the initial yield strength (Figure 9a). The smallest initial yield strength in this study is 350 Pa for a maximum initial landslide thickness $D = 20 \text{ m}$, $V = 0.04 \text{ km}^3$, $F = 0.05$, $\theta = 3.02$, $d_F = 0.316$, and $a/b = 2.33$. The largest τ_{y0} in this study is 1,340 kPa for $D = 1,680 \text{ m}$, $V = 125 \text{ km}^3$, $F = 0.65$, $\theta = 11.77$, $d_F = 3.16$, and $a/b = 0.47$.

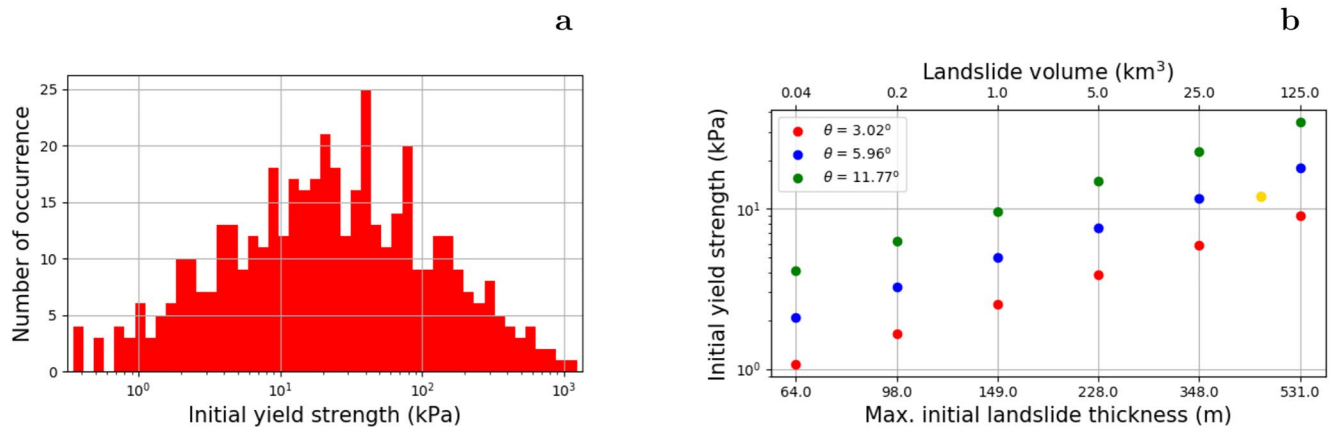


Figure 9. (a) Initial yield strength τ_{y0} displayed in a histogram with 450 events. The approach of scaling the initial yield strength based on the factor of safety yields a large span in its values. (b) Initial yield strength versus landslide volume and initial maximum landslide thickness by using $d_f = 1.0$, $F = 0.05$, and $alb = 1.04$. The yellow dot represents an equivalent of the Storegga Slide with same initial yield strength $\tau_{y0} = 12$ kPa and initial maximum landslide thickness $D \approx 450$ m, but smaller landslide volume.

While we acknowledge that a small subset of these may result in almost artificially low yield strength values, they are nevertheless useful for a broad assessment of the sensitivity of this landslide material parameter. We also remark that one reason for the rather low initial yield strength values is that modeled landslides are already assumed to be pre-remoulded when the slide motion starts, and is hence expected to have lower values than based on core samples measured in the laboratory. The residual yield strength spans from 43.8 Pa to 670 kPa based on $2 < f < 8$ in this study.

There are just a few previous hindcasts of past landslides using Bingclaw and similar models, yet, for a comparison, Kim et al. (2019) found that $\tau_{y0} = 12$ kPa and $\tau_{yr} = 3$ kPa fitted landslide run-out and tsunami runup induced by the Storegga Slide with $V = 3,500$ km³ and $D \approx 450$ m. Figure 9b shows that the example of the Storegga Slide lies within the range of our landslide parameter values (initial yield strength and initial landslide thickness). The Storegga Slide rheology is, in relation to our study, near to a landslide with an initial yield strength of 9 kPa for a regular thick landslide ($d_f = 1.0$) with $D = 531$ m for the largest applied landslide volume, $V = 125$ km³, and a factor of safety $F = 0.05$. This indicates that the values of yield strengths used by Kim et al. (2019) are within our applied range. Snelling et al. (2020), on the other hand, applied yield strengths ranging from 0 to 20 kPa, which cover only the softest range of the landslide materials.

The parameter value ranges for the hydrodynamic resistance parameters are centered around $C_F = 0.01$, $C_p = 1$, and $C_m = 0.1$, following Kim et al. (2019). We add values that are one order of magnitude larger and smaller to investigate the model sensitivity (see Table 1). We further use parameter values of $\Gamma = 0.0005, 0.005, 0.05$ based on previous case studies on the Storegga (Løvholm et al., 2017), Grand Banks (Løvholm et al., 2018; Zengaffinen, Løvholm, Pedersen, & Harbitz, 2020), and South China Sea (Ren et al., 2019) submarine landslide events.

5.3. Model Sensitivity and Comparison With Run-Out Ratios

We start analyzing the sensitivity to the thickness factor d_f . Deep-seated landslides (large d_f) are restricted in their horizontal displacement, and therefore do not completely flow out of their source area and therefore often behave more like rotational slumps (as modeled in, e.g., Zengaffinen, Løvholm, Pedersen, and Harbitz (2020)). Slump-like behavior is particularly evident for the highest safety factors and lowest sensitivity values. Figure 10a shows the sensitivity of the run-out distance and compares the results with the observed landslide run-out in the Gulf of Cadiz. We see that varying d_f alone cannot span the full range of run-out ratios (H'/L) in the data, however, the range of run-out distances (not scaled with H') in the Gulf of Cadiz is covered with the simulations (results not shown). Simulated peak mean landslide velocities (Figure 11a) increase with increasing landslide volume and decreasing d_f . Hence, thin landslides (low d_f) produce larger velocities than deep-seated ones such as slumps.

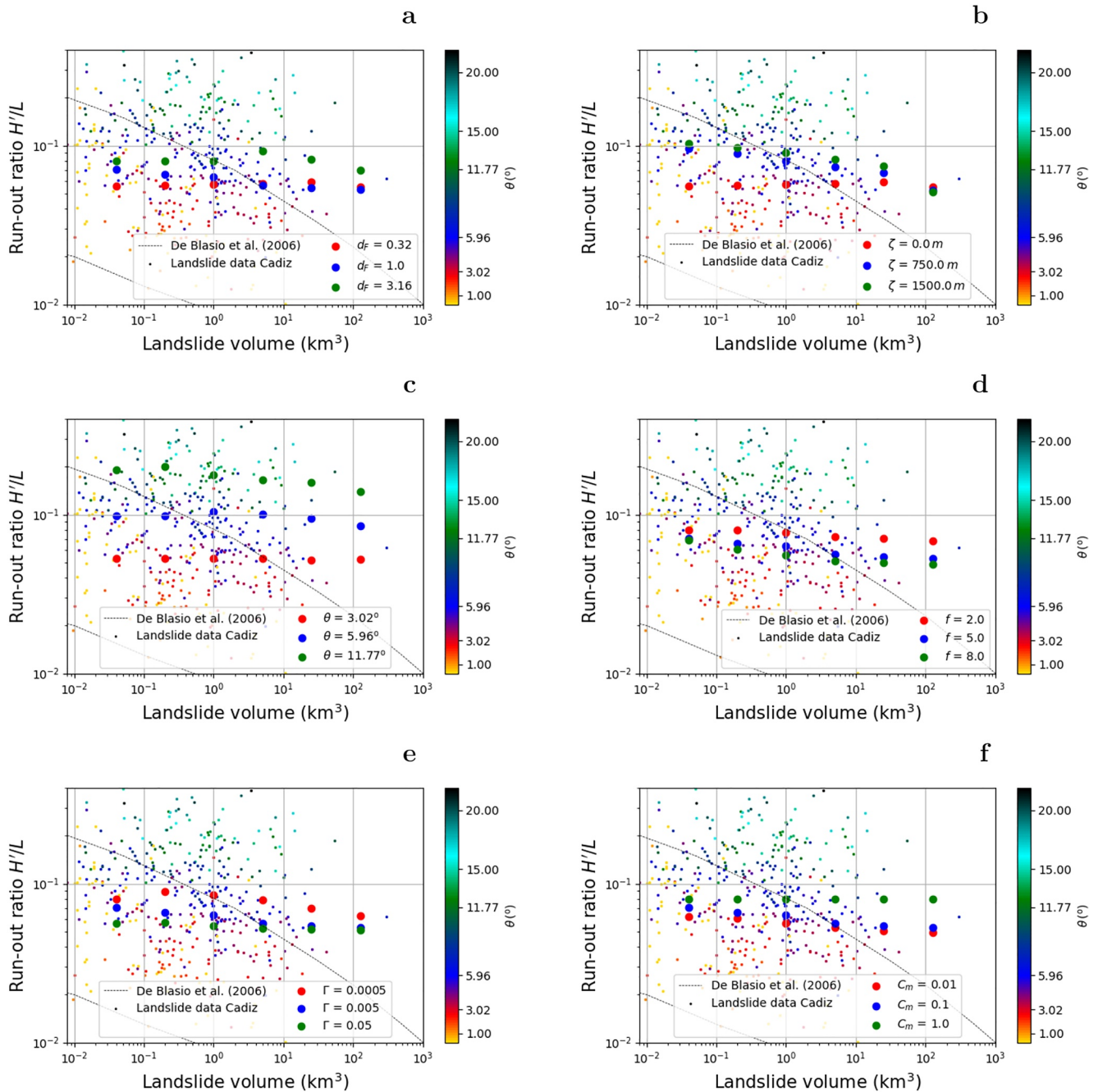


Figure 10. Comparison of simulated run-out ratios H'/L in the idealized geometries with observations from the Gulf of Cadiz. (a) Sensitivity to d_f . (b) Sensitivity to ζ . (c) Sensitivity to θ . (d) Sensitivity to f . (e) Sensitivity to Γ . (f) Sensitivity to C_m . The fixed landslide parameter values, if not investigated, are $d_f = 0.316$ (for panels [a–c]), $d_f = 1.0$ (for panels [d–f]), $\theta = 3.02^\circ$, $\zeta = 0$, $a/b = 1.04$, $F = 0.65$, $f = 5$, $\Gamma = 0.005$, $C_p = 0.01$, $C_p = 1.0$, and $C_m = 0.1$.

A similar observation is found for the run-out distances investigating the sensitivity to ζ , which is simply an effect of moving the masses up-slope. The larger drop heights imply larger H' values and related H'/L values. All simulation results lie inside the observations in the run-out ratio plot (Figure 10b). In general, the run-out ratio decreases with decreasing ζ for small landslide volumes. The sensitivity to ζ becomes smaller the larger the landslide volume is. Overall, H'/L seems more sensitive to ζ than to d_f , but also varying this slope parameter alone is not sufficient to span the observed H'/L range.

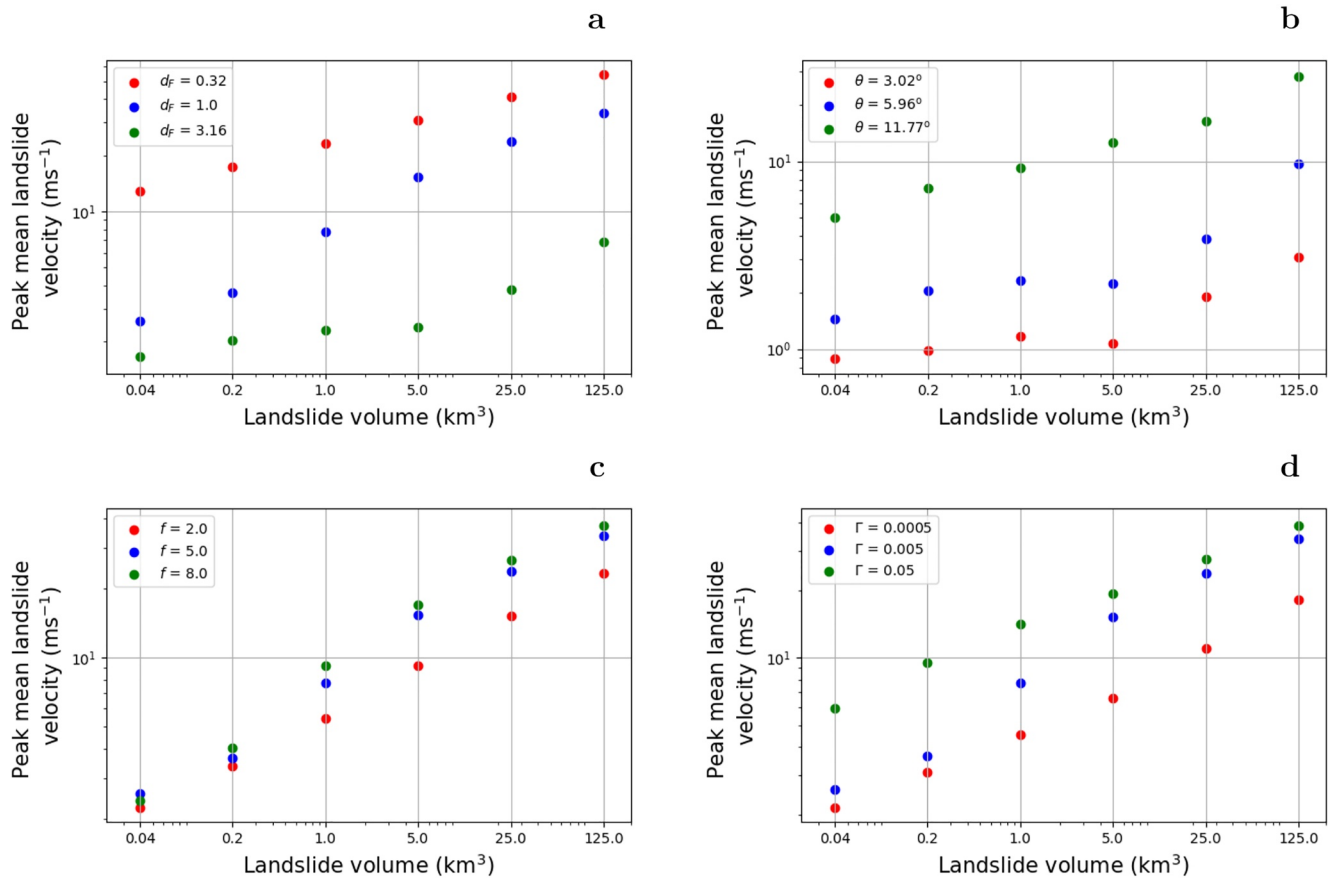


Figure 11. Sensitivity of the peak mean landslide velocity to different geometric and material landslide parameters. (a) sensitivity to d_f (b) sensitivity to θ . (c) sensitivity to f (d) sensitivity to Γ . The fixed landslide parameter values, if not investigated, are $d_f = 0.316$, $\theta = 5.96^\circ$, $ab = 1.04$, $F = 0.65$, $f = 5$, $\Gamma = 0.005$, $C_F = 0.01$, $C_p = 1.0$, and $C_m = 0.1$.

Out of the different sensitive landslide parameters investigated, we find that the modeled run-out ratio is most sensitive to the slope angle θ (Figure 10c). Short run-out landslides are initiated on steep slopes and hence do not flow all the way to the basin floor, thus produce large run-out ratios. Figure 11b shows that the peak mean velocity increases with landslide volume and slope angle. A slope angle increase from 3° to 6° implies more than doubling the velocity for the largest landslides.

We found that the initial yield strength has a small influence on the run-out distance (results not shown). On the other hand, we find a larger sensitivity to the remoulded yield strength, and thus to the sensitivity parameter f . The velocities are generally higher for landslides with lower residual yield strength, and the peak mean velocity occurs after the center of mass has been entirely remoulded. Figure 11c shows peak mean velocities for all six different landslide volumes illustrating that the lower the residual yield strength, meaning higher soil sensitivity f , the larger is the peak velocity. The peak mean velocity for the largest landslide is around 35 m s^{-1} . Larger run-out ratios imply also shorter run-out distances, relatively speaking, because each landslide has the same vertical drop height for various τ_y . Based on Figure 10d we further find that a lower remoulded yield strength causes smaller run-out ratios, but we see that this landslide material parameter only spans a small part of the H'/L range. We note that in previous studies (e.g., Kim et al., 2019) a pronounced effect of f on the total run-out distance L was found. Hence, some influence of the sensitivity f should be expected, in particular for other landslide parameter combinations not tested in this simple sensitivity analysis.

Run-out ratios for various remolding rates Γ are shown in Figure 10e, displaying a moderate sensitivity to H'/L , yet higher than for f . Figure 11d shows that the remolding has a pronounced effect also on the peak landslide velocities.

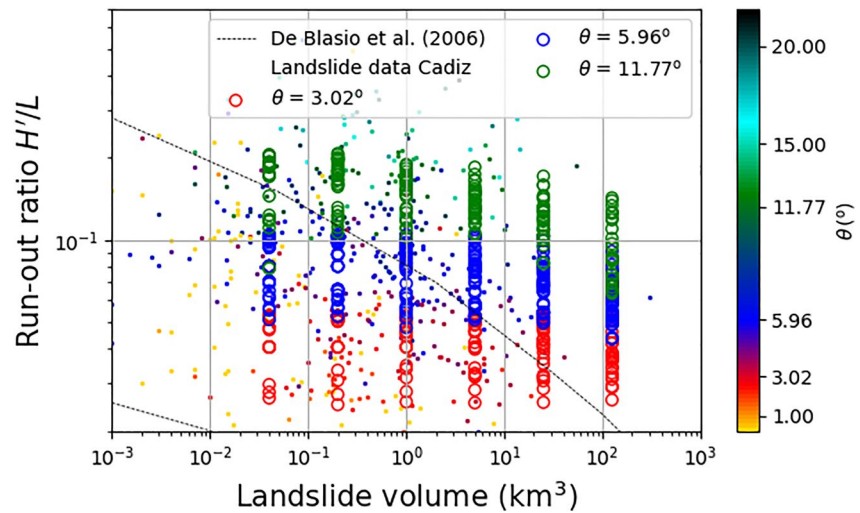


Figure 12. Landslide volume versus run-out ratio for all investigated slope parameter ranges of V , d_F , θ , and ζ , and for selected landslide material parameter combinations for f , Γ , and C_m as shown in Figure 10. Other landslide parameters that have fixed values in this plot, are marked as bold in Table 1. The field marked with dashed line represents the scatter in H'/L versus volume for submarine landslides from De Blasio et al. (2006). The slope angle at the source, θ , is color-coded in both the simulation results (circles) and in the submarine landslide catalog of the Gulf of Cadiz (dots). Simulation results cover the observed data well.

We have also investigated the sensitivities to the pressure drag coefficient C_p , friction drag coefficient C_F , and added-mass coefficient C_m . Decreasing values imply smaller hydrodynamic resistance forces implying that the landslide can move at higher speeds (lower C_p and C_F values) and accelerate faster (lower C_m values). We show the sensitivity to the run-out ratio for the added-mass coefficient C_m in Figure 10f. Run-out ratios decrease with increasing landslide volume and with decreasing C_m . The run-out ratios for $C_m = 1.0$ are nearly constant for all landslide volumes.

In Figure 12, we show the modeled run-out ratios for all the geometric model combinations for V , d_F , θ , and ζ . In the individual landslide parameter sensitivity plots in Figure 10 we show only a selection of these combinations. Hence, the overall variability combining all landslide parameters in Figure 12 is larger than in the individual sensitivity plots alone. The selected landslide material parameter combinations we use in Figure 12 are based on the parameter values used in Figure 10. The individual sensitivity studies shown in Figures 10 and 11 clearly show that the slope parameters, and in particular the slope angle θ are more important than landslide material parameters for explaining the run-out ratios. Snelling et al. (2020) reported similar findings. On the other hand, the slope parameters such as the slope angle and the water depth, for instance, will not appear equally uncertain as the landslide material parameters in, for instance, a probabilistic hazard analysis. The reason is that slope parameters are known for a specific landslide location, however, this is not the case for the landslide material parameters.

6. Influence of Landslide Parameters on Tsunami-Genesis and Related Uncertainty

The landslide dynamics simulations carried out in Section 5 cover the range of observed landslide run-out ratios in the Gulf of Cadiz and probably that of many other fully submarine and lacustrine environments (likely a subset of the parameters covered here), given the non-dimensional approach and the range of volumes, H'/L ratios and rheologies covered in this study. Here, we use the same landslide simulation setup as input to tsunami simulations to investigate how uncertain the related tsunami-genesis is using the setup outlined in Section 3.4. We note here that the outcome of these simulations is rather specific for the slope characteristics reported in Figure 3, inspired by the Gulf of Cadiz continental margin, nevertheless several other continental margins worldwide have similar geometry. A complicating factor is that different landslide parameters control landslide run-out distance and tsunami-genic strength (e.g., Kim et al., 2019). Hence, we must explore the sensitivity to an additional set of

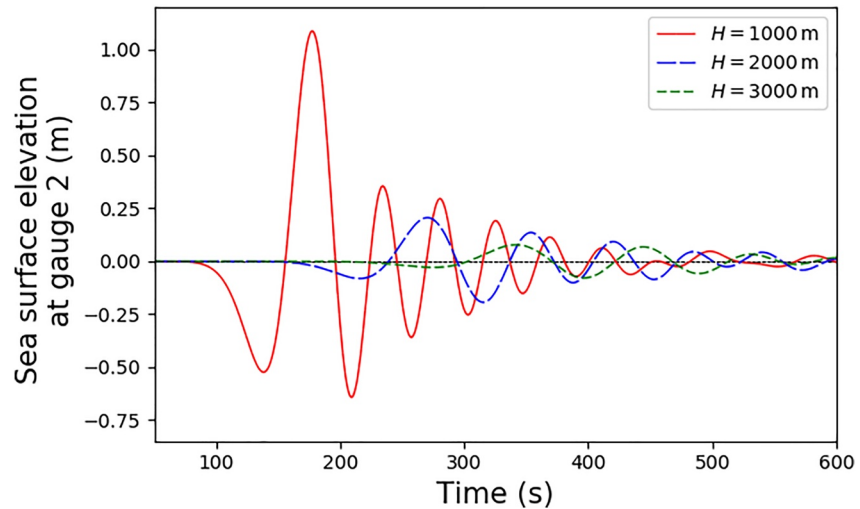


Figure 13. Time series of the sea surface elevations at gauge 2 (see Figure 3) for landslides originating at various water depths. Applied landslide parameters are $V = 1 \text{ km}^3$, $d_F = 3.16$, $\zeta = 0 \text{ m}$, $\theta = 5.96^\circ$, $a/b = 1.04$, $F = 0.65$, $f = 5$, $\Gamma = 0.005$, $C_F = 0.01$, $C_P = 1.0$, and $C_m = 0.1$.

parameters when addressing tsunami uncertainty compared to the investigations of the run-out distances carried out above.

6.1. Effects of Geometric, Rheological, and Hydrodynamic Resistance Parameters on Tsunami-Genesis

First, we exemplify the effect of a single landslide parameter, namely how the initial center water depth of the landslide (H) influences the tsunami genesis. To test the role of H in tsunami-genesis, we set the landslide failure to originate at various initial landslide water depths $H = 1,000, 2,000, 3,000 \text{ m}$. Figure 13 shows the time series of the sea surface elevations at gauge 2 (η_{c2} ; see Figure 3) for the three different water depths for a landslide of 1 km^3 in volume (Figure 13 caption for additional landslide parameters). The shallower the landslide is located, the more efficient the tsunami genesis is in producing higher surface elevations. Halving the water depth from 2000 to 1,000 m implies a five times larger maximum elevation for this example. The wave period is shorter for the shallower landslides, and the tsunami arrival times are different for the landslide at various water depths, because of the geometrical setup used in this study (Figure 3).

Figure 14a shows sensitivity of the maximum sea surface elevations η_{c2} to the initial water depth for various landslide volumes, displaying also an expected increasing tsunami-genetic strength with increasing volume. The tsunami is highly sensitive to the water depth for all volumes, but the sensitivity is largest for the smallest volumes. This may be explained by larger volumes being distributed over a larger area with a greater span in water depth. The sensitivity to the source length-to-width ratio a/b is shown in Figure 14b. Wider landslides with the same volume ($a/b > 1$) produce higher (but more focused) tsunamis than landslides with $a/b < 1$. Further, we show the sensitivity to the landslide source slope angle θ in Figure 14c. As for the water depth, a strong effect of the slope angle on the tsunami-genesis is observed. We also investigated the effect of the thickness factor d_F but did not find a systematic trend with respect to the tsunami-genesis (results not shown).

Next, we investigate the sensitivity of the induced tsunami surface elevation to the landslide dynamics for different parameters. The landslide material parameter that is most sensitive to the maximum sea surface elevation is the initial yield strength of the landslide material τ_{y0} , here indirectly compared with the tsunami surface elevation by the factor of safety F . To this end, we note that, as F incorporates other elements such as the shape of the landslide and the slope angle, it is hence not a direct measure of the material strength only. Figure 15a shows increasing maximum sea surface elevation η_{c2} with decreasing F , implying that softer initial landslide masses are more tsunamigenic than stiffer masses. The other two landslide material parameters representing the material yield strength, the remolding rate Γ and the residual yield strength of the landslide mass $\tau_{y,r}$, did not influence

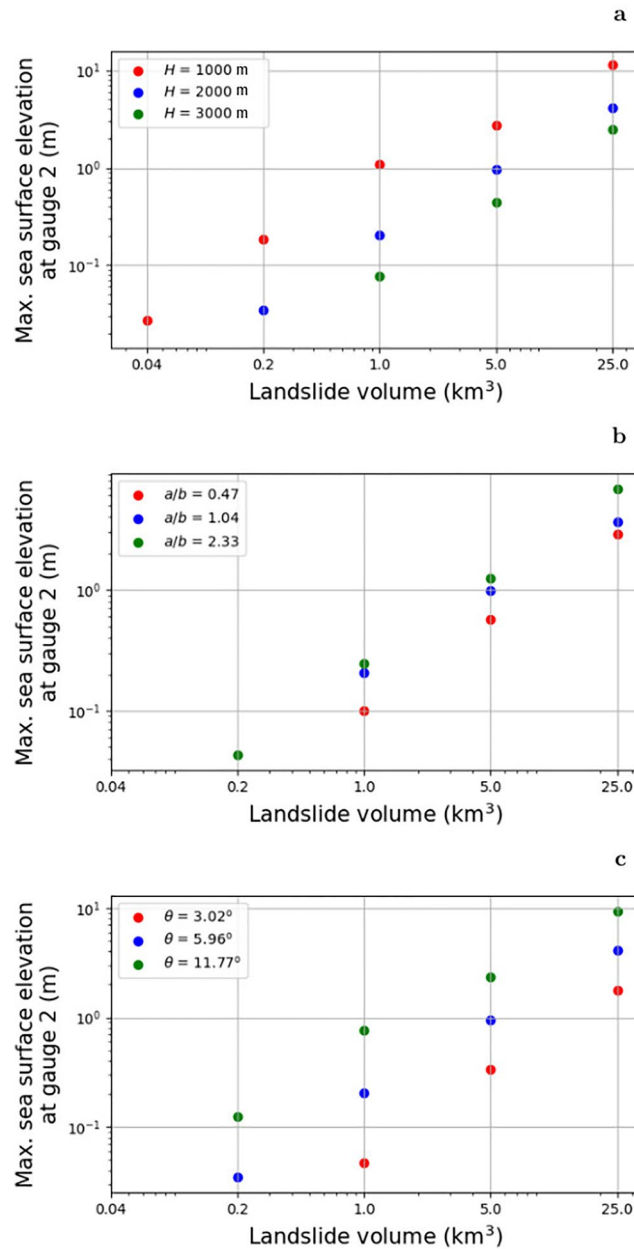


Figure 14. Landslide volume versus maximum sea surface elevation at gauge 2 with (a) various H , (b) various a/b , (c) various θ . Applied landslide parameters are $H = 2,000$ m except in (a), $d_F = 3.16$ except in (d), $\zeta = 0$ m, $\theta = 5.96^\circ$ except in (c), $a/b = 1.04$ except in (b), $F = 0.65$, $f = 5$, $\Gamma = 0.005$, $C_F = 0.01$, $C_P = 1.0$, and $C_m = 0.1$.

the maximum sea surface elevation significantly (results not shown). We note that this finding is consistent with previous results (Kim et al., 2019) showing that the tsunami-genesis is controlled by τ_{y0} and the run-out is controlled by the residual yield strength τ_y .

Increasing hydrodynamic resistance parameters C_m , C_F , and C_P reduces the sea surface elevations. We found that the tsunami-genesis was most sensitive to the added-mass coefficient C_m . Figure 15b exemplifies the related sensitivity to C_m . For the largest C_m value, η_{c2} is one order of magnitude smaller than for the smallest C_m value. On the other hand, we note that C_m scales with the size of the landslide (see Kim et al., 2019), and that $C_m = 1$ is likely a much too large value for the greatest landslide volumes. For the further analysis below, we use only

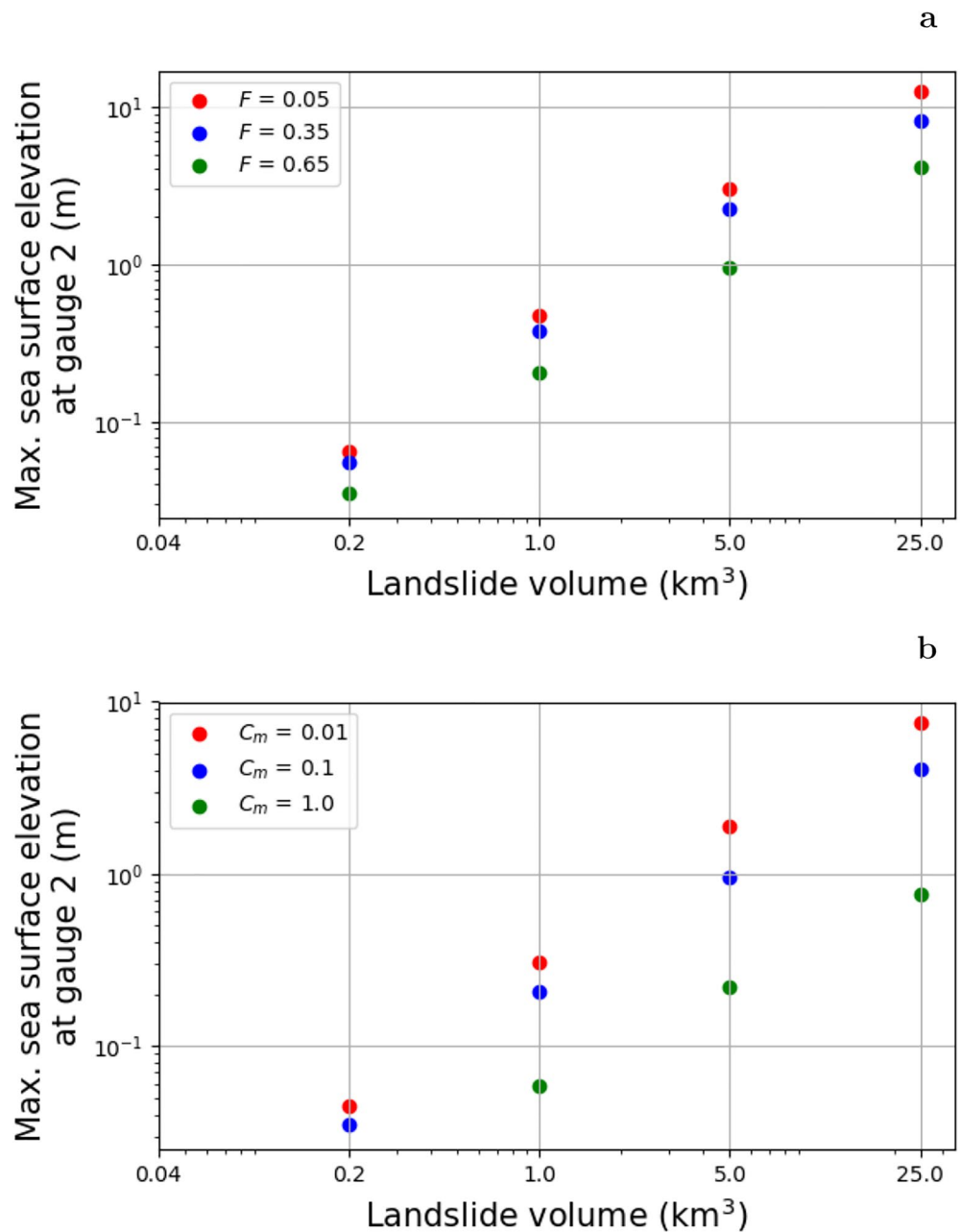


Figure 15. Landslide volume versus maximum sea surface elevation at gauge 2 with (a) various F and (b) various C_m . Applied landslide parameters are $H = 2,000$ m, $d_F = 3.16$, $\zeta = 0$ m, $\theta = 5.96^\circ$, $alb = 1.04$, $F = 0.65$ only in (b), $f = 5$, $\Gamma = 0.005$, $C_F = 0.01$, $C_p = 1.0$, and $C_m = 0.1$ only in (a). The maximum sea surface elevation increases with increasing landslide volume V , decreasing F , and decreasing C_m .

$C_m = 0.1$ for computational feasibility. C_F and C_p had a smaller influence on the maximum sea surface elevation η_{e2} at gauge 2, and were hence not investigated in detail (results not shown).

Figure 16 shows the tsunami uncertainty distribution, generated by simulating events with a combination of the sensitive input landslide parameters discussed above, V , alb , H , θ , d_F , and F . C_m sensitivity was not included as this would render the numbers of simulations infeasible. The other, less sensitive landslide parameters have fixed values that are marked in bold in Table 1. Maximum sea surface elevations increase with increasing landslide volume. However, the tsunami surface elevations span 1.5–2.5 orders of magnitude for a fixed landslide volume. This shows that, by calibrating the landslide parameters from the static run-out observations, the uncertainty in

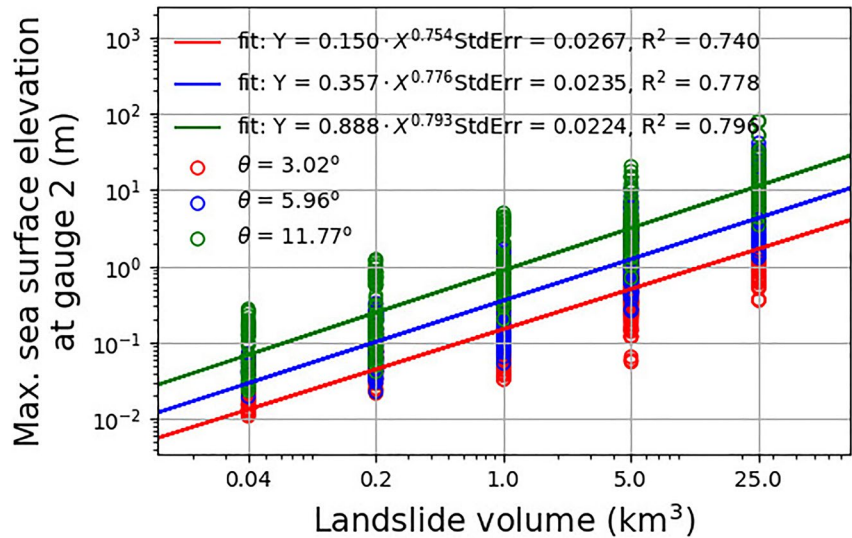


Figure 16. Landslide volume versus maximum sea surface elevation at gauge 2 for the most sensitive landslide parameters to tsunami genesis, V , alb , H , θ , d_f , and F . Other landslide parameters that have fixed values in this plot, are marked as bold in Table 1. The large scatter in the simulation results implies significant tsunami uncertainty based on the statistical slope parameter ranges from the landslide database.

the maximum sea surface elevations can be excessive if no further attempt is made to correlate the tsunami-genesis with other variables in addition to the volume. Fortunately, as explained below, some reduction of this uncertainty is possible. Arguably, the most sensitive landslide parameter is the slope angle at the source, and the coloring in Figure 16 illustrates this sensitivity.

In order to explain the relatively large uncertainty in simulated maximum sea surface elevations, we establish parametric relationships between important landslide parameters and the maximum elevation η_{c2} at gauge 2. The parameterization is carried out on a trial and error basis. We use integer exponents for the slope parameters V , $\sin\theta$, H , alb , and d_f and found that the results were less sensitive to alb and d_f , so these slope parameters were left out of the parametric relationship. For the landslide material parameter F we use one-digit floating exponents, because tsunami genesis is less sensitive to landslide material parameters than slope parameters. Additional sensitivity to the hydrodynamic resistance parameters C_m , C_F , and C_P is expected. Testing different values for each exponent for V , H , alb , $\sin\theta$, d_f , and F finally resulted in the smallest standard error of $6.7 \cdot 10^{-3}$ and the largest correlation coefficient $R^2 = 0.95$ from linear regression analysis. Figure 17a shows all simulations fitted to the resulting power law expression:

$$\eta_{c2} = k \left(\frac{(\sin\theta)^2 V}{H^2 F^{0.3}} \right)^m \quad (9)$$

where $k = 0.073$ and the power law exponent $m = 0.89$.

The relation given in Equation 9 shows that the greatest control on the tsunami variability is given by the slope parameters $\sin\theta$ and H . Despite this, there is still a pronounced uncertainty in the tsunami-genetic strength in Figure 17a, but the uncertainty is dramatically reduced compared to Figure 16 where there is no attempt to use slope and landslide material parameters to explain the tsunami-genesis. When excluding slope parameters in the scaling relation given by Equation 9, correlating the tsunami surface elevation only with the initial yield strength τ_{y0} and the landslide volume V , a moderate correlation with the maximum sea surface elevation at gauge 2 based on linear regression analysis is obtained, and the data scatter is strongly increased (Figure 17b). On the other hand, the data scatter is clearly smaller than in Figure 16 only correlating the volume to the tsunami-genetic strength. This shows that F also has a significant influence on the tsunami-genesis in addition to H and $\sin\theta$.

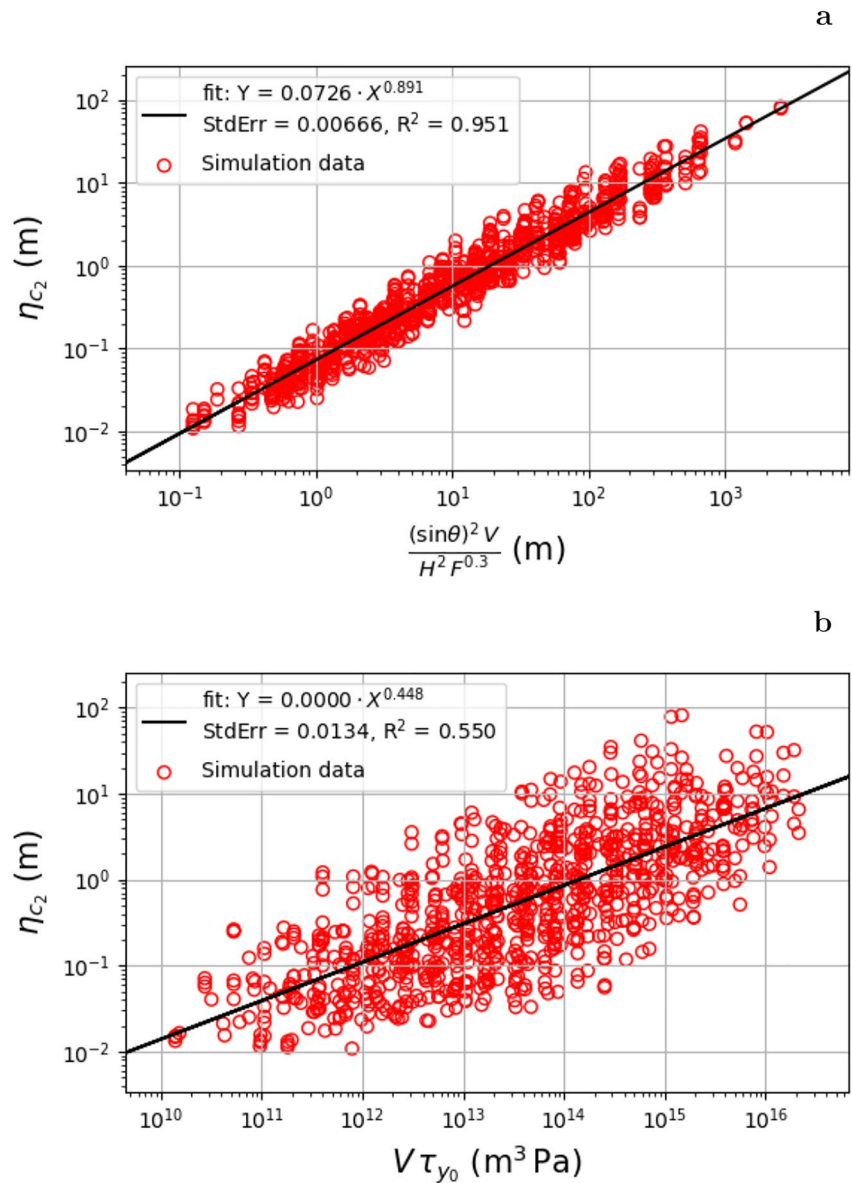


Figure 17. Maximum sea surface elevation at gauge 2 versus (a) scaled landslide parameters based curve fitting and (b) landslide volume multiplied by the initial yield strength. The scaling correlation is strong in (a) and moderate in (b). X refers to the X -axis and Y to the Y -axis. StdErr is the least squares standard error. Constant landslide parameters are $\zeta = 0$ m, $f = 5$, $\Gamma = 0.005$, $C_F = 0.01$, $C_P = 1.0$, and $C_m = 0.1$.

The tsunami wavelength is also sensitive to certain landslide parameters. We estimate here the wavelength from the product of the hydrostatic wave speed with the wave period of the leading wave extracted at gauge 2. The wave period of the leading wave is defined as the time difference between the time of the second zero-crossing and when the sea surface elevation drops first below a threshold value of 1 mm, and hence based on the first wave arrival only. Figure 18 shows the correlation with the leading wavelength at gauge 2 of the product of the water depth squared H^2 , the landslide volume V , divided by the product of the ratio a/b , and the thickness factor squared $(d_F)^2$. This scaling law is based on the same trial and error curve fitting procedure as done for the maximum sea surface elevation. We find a correlation $R^2 = 0.76$ based on this relationship.

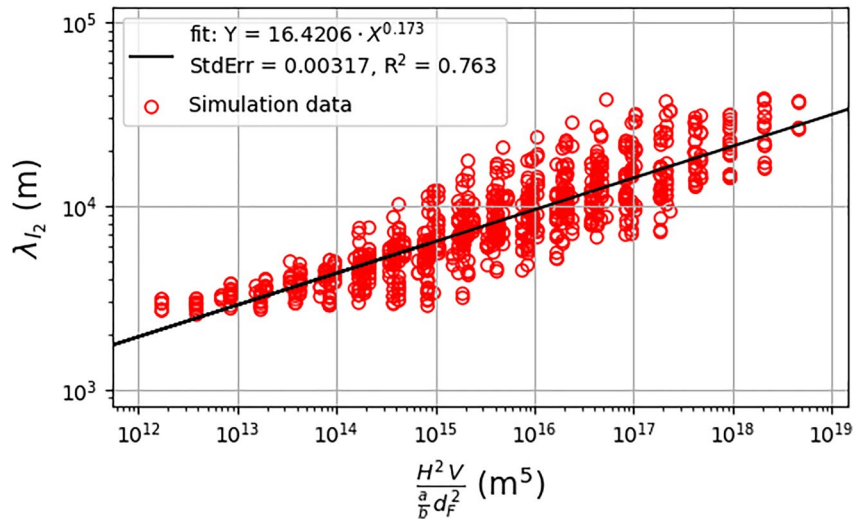


Figure 18. Leading wavelength at gauge 2, λ_{l_2} , versus a combination of landslide parameters showing a moderate correlation. X refers to the X -axis and Y to the Y -axis. StdErr is the least squares standard error. Constant landslide parameters are $\zeta = 0$ m, $f = 5$, $\Gamma = 0.005$, $C_F = 0.01$, $C_p = 1.0$, and $C_m = 0.1$.

6.2. Relationships Between Kinematic Landslide Properties and Tsunami Genesis

Alternatively to scaling the tsunami sea surface with landslide material parameters, we may relate the tsunami-genic strength to landslide kinematics, determined a posteriori (after landslide release). We first define the Froude number according to:

$$Fr = v_{peak}^{mean} / \sqrt{gH} \equiv v_{peak}^{mean} / c_0 \quad (10)$$

using the hydrostatic wave speed $c_0 = \sqrt{gH}$ at the mean initial water depth of the landslide, and slope parameters. All landslides are sub-critical, implying that they move slower than the hydrostatic wave speed, as $Fr < 0.7$ for all simulations in this study, but mostly much less as Fr is reduced when the landslide moves into deep water. As in the power law of Equation 9, we perform a curve fit using integer exponents for slope parameters, including the Froude number. Based on linear regression analysis, the smallest standard error using the mean peak velocity is 0.0075 with $R^2 = 0.87$. This indicates a strong correlation between η_{c_2} and $\left(Fr_{peak}^{mean}\right)^2 \frac{a}{b} (d_F)^2 V (c_0)^{-2}$. This power law relationship reads:

$$\eta_{c_2} = k_{Fr}^{mean} \left(\frac{\left(Fr_{peak}^{mean}\right)^2 \frac{a}{b} (d_F)^2 V}{(c_0)^2} \right)^{m_{Fr}^{mean}} \quad (11)$$

where $k_{Fr}^{mean} = 0.0087 \text{ m (m s}^{-2}\text{)}^{-m_{Fr}^{mean}}$ and $m_{Fr}^{mean} = 0.59$ (Figure 19a).

A similar curve fit as for the Froude number is applied to the initial acceleration. The standard error using the mean initial acceleration is 0.0067 with $R^2 = 0.95$, meaning strong correlations between η_{c_2} and $(a_0^{mean})^2 V (c_0)^{-4}$. The initial acceleration embeds in a power law with the maximum sea surface elevation according to

$$\eta_{c_2} = k_a^{mean} \left(\frac{(a_0^{mean})^2 V}{(c_0)^4} \right)^{m_a^{mean}} \quad (12)$$

where $k_a^{mean} = 2.35 \text{ m}^{-m_a^{mean}}$ and $m_a^{mean} = 0.84$ (Figure 19b).

Other authors such as Harbitz et al. (2006), Haugen et al. (2005), and Løvholt et al. (2005) found similar scaling relationships with the maximum sea surface elevation for moving blocks, of the form $\sim \frac{V a_0}{(c_0)^7}$. Zengaffinen, Løvholt, Pedersen, and Harbitz (2020) also found a similar scaling relationship for slumps. Similar to Zengaffi-

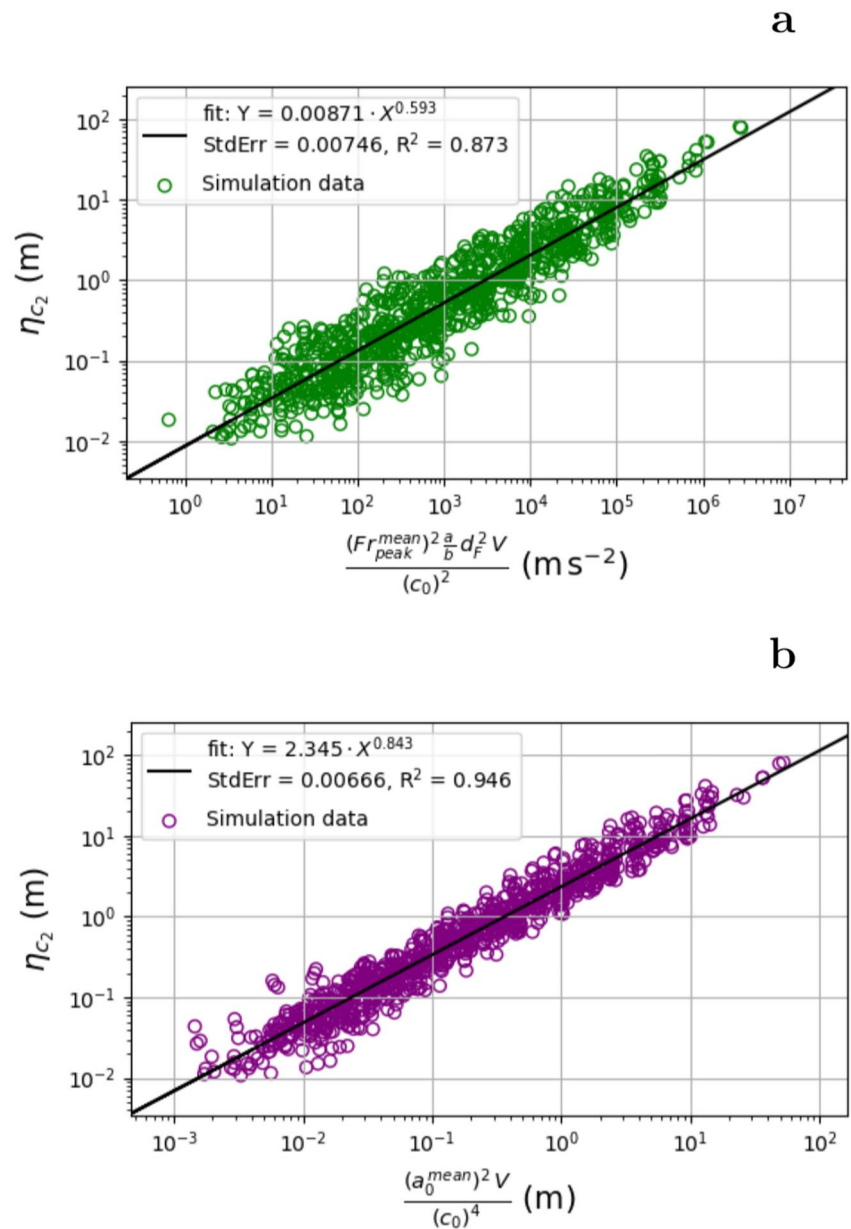


Figure 19. Scaled landslide volume versus maximum sea surface elevation at gauge 2, η_{c_2} . The scaling includes (a) the Froude number Fr_{peak}^{mean} based on the peak mean landslide velocity and (b) the initial mean landslide acceleration a_0^{mean} . Both kinematic quantities scale proportionally with η_{c_2} , and show, combined with slope parameters, a strong correlation with η_{c_2} . Constant landslide parameters are $\zeta = 0$ m, $f = 5$, $\Gamma = 0.005$, $C_F = 0.01$, $C_p = 1.0$, and $C_m = 0.1$. X refers to the X -axis and Y to the Y -axis. StdErr is the least squares standard error.

nen, Løvholt, Pedersen, and Harbitz (2020), we here find a more linear relationship with a_0 (scaled with the water depth) than Fr . However, in this study we investigate a much broader range of landslides, and the relationships are believed to be more generic.

7. Concluding Remarks

We have compiled a new database for the Gulf of Cadiz, and analyzed the statistics of these data. The cumulative-volume distribution follows a power law for the larger landslide volumes. Slope parameters such as the mean source slope angle and the source area width to length ratio follow a lognormal distribution. We found no upper limit in the data for the run-out ratio H'/L for submarine landslides as De Blasio et al. (2006) did, thus we suggest

that there is pronounced overlap between subaerial and submarine landslides in terms of run-out ratio H/L (interpreted as apparent friction coefficient). Nonetheless, a significant number of submarine landslides display lower values of the run-out ratio compared to subaerial landslides thus pointing to differences in flow mechanics between submarine and subaerial landslides.

A large set of landslide simulations with simplified geometric landslide and bathymetric configurations using the depth-averaged cohesive landslide model BingClaw have been carried out. These simulations cover the wide range of observed landslide run-out ratios in the Gulf of Cadiz through a set of plausible slope and landslide material parameters, including hydrodynamic resistance, in BingClaw. To make the computations feasible, a simplified geometric setup was used. Based on this modeling that covers the large statistical scatter in observed run-out ratios, we have used the simulations to constrain landslide material parameter uncertainty ranges such as the remoulded yield strength τ_{y_r} .

As the range of run-out ratios are broadly compatible with information extracted from the landslide database from the Gulf of Cadiz, we assume that the constrained ranges for the landslide material parameters can represent a first pass range as input to a tsunami model. The parameter range represents the epistemic uncertainty of the landslide material parameters, obtained by combining static landslide run-out observations and the dynamic landslide model BingClaw. While this uncertainty range may be excessively large, it still represents the best estimate we have for these parameters, as covering the entire area with geotechnical measurements is not feasible.

Based on the landslide simulations with related constrained landslide parameters, we coupled the numerical landslide model to tsunami simulations. With the wide range of landslide parameters necessary to span the observed run-out ratios, we also obtain a wide range of maximum sea surface elevations based on the same landslide simulations. The large uncertainty in these elevations can be explained by the sensitivity to variable slope parameters and landslide material parameters such as the initial yield strength. By carrying out a simple correlation study relating non-linear properties, such as the water depth and slope angle of the initial landslide source area, and the geotechnical safety factor, we were able to reduce this variability significantly, and parameterize the source strength. As in previous studies, we also find relationships between kinematic properties, such as the Froude number and the initial landslide acceleration, and the maximum sea surface elevation.

The results of the simulated tsunami uncertainties, presented in Figures 16 and 17, constitute the baseline for a future landslide probabilistic tsunami hazard analysis (LPTHA). Figure 16 relates the tsunami surface elevation to the landslide volume only, with significant uncertainty, while Figure 17 shows that the uncertainty can be drastically reduced by taking into account bathymetric effects and initial landslide yield strength. As explained above, the uncertainty in landslide parameters is anchored toward landslide observations. On the other hand, the landslide material parameters that control tsunami-generation do not coincide one-to-one with those that determine the landslide run-out. Hence, there is further need to understand the epistemic uncertainty in the material parameters. On the other hand, the present study investigates a rather broad range of such parameters, including the initial yield strength and several hydrodynamic resistance parameters. In future efforts, the present analysis will be integrated with landslide source statistics, geotechnical susceptibility maps (Collico et al., 2020), and tsunami simulations using actual bathymetry. We note that such effort, along with understanding landslide tsunami uncertainty, ranks among the most important research gaps as judged by the tsunami research community (Behrens et al., 2021). Completing a LPTHA is by no means a trivial task, and the uncertainty treatment will require high performance computing facilities. To this end however, the present analysis shows that the landslide source uncertainty can be clearly reduced compared to previous knowledge, which will help for the feasibility of future understanding of submarine landslide tsunami hazards.

Data Availability Statement

The following key data set are used and made available in this paper: The new landslide database covering the Gulf of Cadiz is available through the following repository (Urgeles et al., 2021). The main outputs from the simulation, that is, those displayed in in Figures 9–12 and 14–19 are available through (Zengaffinen-Morris, 2022). The landslide model BingClaw has been published previously in the AGU journal Geophysical Research Letters, with the availability statement given in (Løvholt et al., 2017). Please note that the entire data set resulting from the model simulations, exceed 1 TB and is hence too large to place in a public repository. Hence, only the main outputs from the simulations are made available here.

Acknowledgments

This project has received funding from the European Union's Horizon 2020 research and innovation program under the Marie Skłodowska-Curie grant agreement No. 721403. The Spanish "Ministerio de Ciencia e Innovación" and the European Regional Development Fund through grant CTM2015-70155-R (project INSIGHT) and Expert Analytics AS in Oslo are also acknowledged. Early stage researcher William Meservy is gratefully acknowledged for useful discussions on the landslide database. Finally, we thank Michael Strupler and one anonymous reviewer for their helpful reviews of the manuscript.

References

Banda, E., Torne, M., & Group, I. A. M. (1995). Iberian Atlantic Margins Group investigates deep structure of ocean margins. *Eos, Transactions American Geophysical Union*, 76(3), 25–29. <https://doi.org/10.1029/EO076i003p00025>

Baptista, M. A., Heitor, S., Miranda, J. M., Miranda, P., & Victor, L. M. (1998). The 1755 Lisbon tsunami; evaluation of the tsunami parameters. *Journal of Geodynamics*, 25(1–2), 143–157. [https://doi.org/10.1016/S0264-3707\(97\)00019-7](https://doi.org/10.1016/S0264-3707(97)00019-7)

Baptista, M. A., & Miranda, J. M. (2009). Revision of the Portuguese catalog of tsunamis. *Natural Hazards and Earth System Sciences*, 9(1). <https://doi.org/10.5194/nhess-9-25-2009>

Bartolome, R., Gràcia, E., Stich, D., Martínez-Loriente, S., Klaeschen, D., de Lis Mancilla, F., et al. (2012). Evidence for active strike-slip faulting along the Eurasia-Africa convergence zone: Implications for seismic hazard in the southwest Iberian margin. *Geology*, 40(6), 495–498. <https://doi.org/10.1130/G33107.1>

Behrens, J., Løvholt, F., Jalayer, F., Lorito, S., Salgado-Gálvez, M. A., Sørensen, M., et al. (2021). Probabilistic tsunami hazard and risk analysis: A review of research gaps. *Frontiers of Earth Science*, 9, 114.

Bondevik, S., Løvholt, F., Harbitz, C., Mangerud, J., Dawson, A., & Svendsen, J. I. (2005). The Storegga slide tsunami—comparing field observations with numerical simulations. In *Ormen Lange—An integrated study for safe field development in the Storegga submarine area* (pp. 195–208). Elsevier. <https://doi.org/10.1016/b978-0-08-044694-3.50021-4>

Bracklenridge, R. E., Hernández-Molina, F. J., Stow, D. A. V., & Llave, E. (2013). A Pliocene mixed contourite-turbidite system offshore the Algarve Margin, Gulf of Cadiz: Seismic response, margin evolution and reservoir implications. *Marine and Petroleum Geology*, 46, 36–50. <https://doi.org/10.1016/j.marpetgeo.2013.05.015>

Brune, S., Ladage, S., Babeyko, A. Y., Müller, C., Kopp, H., & Sobolev, S. V. (2010). Submarine landslides at the eastern Sunda margin: Observations and tsunami impact assessment. *Natural Hazards*, 54(2), 547–562. <https://doi.org/10.1007/s11069-009-9487-8>

Bufo, E., Bezzeghoud, M., Udías, A., & Pro, C. (2004). Seismic sources on the Iberia-African plate boundary and their tectonic implications. *Pure and Applied Geophysics*, 161(3), 623–646. <https://doi.org/10.1007/s00024-003-2466-1>

Bufo, E., De Galdeano, C. S., & Udías, A. (1995). Seismotectonics of the Ibero-Maghreb region. *Tectonophysics*, 248(3–4), 247–261. [https://doi.org/10.1016/0040-1951\(94\)00276-F](https://doi.org/10.1016/0040-1951(94)00276-F)

Carvajal, M., Araya-Cornejo, C., Sepúlveda, I., Melnick, D., & Haase, J. S. (2019). Nearly instantaneous tsunamis following the Mw 7.5 2018 Palu earthquake. *Geophysical Research Letters*, 46(10), 5117–5126. <https://doi.org/10.1029/2019GL082578>

Chaytor, J. D., Uri, S., Solow, A. R., & Andrews, B. D. (2009). Size distribution of submarine landslides along the US Atlantic margin. *Marine Geology*, 264(1–2), 16–27. <https://doi.org/10.1016/j.margeo.2008.08.007>

Clark, P. U., Dyke, A. S., Shakun, J. D., Carlson, A. E., Clark, J., Wohlfarth, B., et al. (2009). The last glacial maximum. *Science*, 325(5941), 710–714. <https://doi.org/10.1126/science.1172873>

Clauset, A., Shalizi, C. R., & Newman, M. E. (2009). Power-law distributions in empirical data. *SIAM Review*, 51(4), 661–703. <https://doi.org/10.1137/070710111>

Collico, S., Arroyo, M., Urgeles, R., Gràcia, E., De Vincenzi, M., & Pérez, N. (2020). Probabilistic mapping of earthquake-induced submarine landslide susceptibility in the South-West Iberian margin. *Marine Geology*, 106296. <https://doi.org/10.1016/j.margeo.2020.106296>

De Blasio, F. V., Elverhøi, A., Engvik, L. E., Issler, D., Gauer, P., & Harbitz, C. (2006). Understanding the high mobility of subaqueous debris flows. *Norwegian Journal of Geology*, 86(3).

De Blasio, F. V., Elverhøi, A., Issler, D., Harbitz, C., Bryn, P., & Lien, R. (2005). On the dynamics of subaqueous clay rich gravity mass flows—The giant Storegga slide, Norway. In *Ormen Lange—An integrated study for safe field development in the Storegga submarine area* (pp. 179–186). Elsevier. <https://doi.org/10.1016/b978-0-08-044694-3.50019-6>

Favalli, M., Boschi, E., Mazzarini, F., & Pareschi, M. T. (2009). Seismic and landslide source of the 1908 straits of Messina tsunami (Sicily, Italy). *Geophysical Research Letters*, 36(16). <https://doi.org/10.1029/2009gl039135>

Ford, J., Urgeles, R., Gràcia, E., & Camerlenghi, A. (2020). Seismic diffraction imaging to better understand the internal fabric of mass-transport complexes: Examples from the Gulf of Cadiz, South West Iberian margin. *Journal of Geophysics*.

Fukao, Y. (1973). Thrust faulting at a lithospheric plate boundary the Portugal earthquake of 1969. *Earth and Planetary Science Letters*, 18(2), 205–216. [https://doi.org/10.1016/0012-821X\(73\)90058-7](https://doi.org/10.1016/0012-821X(73)90058-7)

Gamboa, D., Omira, R., & Terrinha, P. (2021). A database of submarine landslides offshore West and Southwest Iberia. *Scientific Data*, 8, 185. <https://doi.org/10.1038/s41597-021-00969-w>

Gamboa, D., Omira, R., Terrinha, P. (2022). Spatial and morphometric relationships of submarine landslides offshore west and southwest Iberia. *Landslides*, 19, 387–405. <https://doi.org/10.1007/s10346-021-01786-3>

García-Orellana, J., Gràcia, E., Vizcaino, A., Masqué, P., Olid, C., Martínez-Ruiz, F., et al. (2006). Identifying instrumental and historical earthquake records in the SW Iberian margin using 210Pb turbidite chronology. *Geophysical Research Letters*, 33(24). <https://doi.org/10.1029/2006GL028417>

Geissler, W., Matias, L., Stich, D., Carrilho, F., Jokat, W., Monna, S., et al. (2010). Focal mechanisms for sub-crustal earthquakes in the Gulf of Cadiz from a dense OBS deployment. *Geophysical Research Letters*, 37(18). <https://doi.org/10.1029/2010GL044289>

Geist, E. L., & ten Brink, U. S. (2019). Offshore landslide hazard curves from mapped landslide size distributions. *Journal of Geophysical Research: Solid Earth*, 124(4), 3320–3334. <https://doi.org/10.1029/2018jb017236>

Gillespie, C. S. (2014). Fitting heavy tailed distributions: The poweRlaw package. arXiv:1407.3492 [physics, stat]. Retrieved from <http://arxiv.org/abs/1407.3492>

Gràcia, E., Danobeitia, J., Vergés, J., Bartolomé, R., & Córdoba, D. (2003). Crustal architecture and tectonic evolution of the Gulf of Cadiz (SW Iberian margin) at the convergence of the Eurasian and African plates. *Tectonics*, 22(4), 1033. <https://doi.org/10.1029/2001tc901045>

Gràcia, E., Danobeitia, J., Vergés, J., & PARSIFAL-Team. (2003). Mapping active faults offshore Portugal (36 N–38 N): Implications for seismic hazard assessment along the southwest Iberian margin. *Geology*, 31, 832–886. [https://doi.org/10.1130/0091-7613\(2003\)031<0803:mafopn>2.0.co;2](https://doi.org/10.1130/0091-7613(2003)031<0803:mafopn>2.0.co;2)

Gràcia, E., Vizcaino, A., Escutia, C., Asioli, A., Rodes, A., Pallas, R., et al. (2010). Holocene earthquake record offshore Portugal (SW Iberia): Testing turbidite paleoseismology in a slow-convergence margin. *Quaternary Science Reviews*, 29(9–10), 1156–1172. <https://doi.org/10.1016/j.quascirev.2010.01.010>

Gutscher, M.-A., Malod, J., Rehault, J.-P., Contrucci, I., Klingelhoefer, F., Mendes-Victor, L., & Spakman, W. (2002). Evidence for active subduction beneath Gibraltar. *Geology*, 30(12), 1071–1074. [https://doi.org/10.1130/0091-7613\(2002\)030<1071:efasbg>2.0.co;2](https://doi.org/10.1130/0091-7613(2002)030<1071:efasbg>2.0.co;2)

Gylfadóttir, S. S., Kim, J., Helgason, J. K., Brynjólfsson, S., Höskuldsson, Á., Jóhannesson, T., et al. (2017). The 2014 Lake Askja rockslide-induced tsunami: Optimization of numerical tsunami model using observed data. *Journal of Geophysical Research: Oceans*, 122(5), 4110–4122. <https://doi.org/10.1002/2016jc012496>

- Hampton, M. A., Karl, H. A., & Murray, C. J. (2002). Acoustic profiles and images of the Palos Verdes margin: Implications concerning deposition from the White's point outfall. *Continental Shelf Research*, 22(6–7), 841–857. [https://doi.org/10.1016/s0278-4343\(01\)00107-8](https://doi.org/10.1016/s0278-4343(01)00107-8)
- Harbitz, C. B., Løvholt, F., & Bungum, H. (2014). Submarine landslide tsunamis: How extreme and how likely? *Natural Hazards*, 72(3), 1341–1374. <https://doi.org/10.1007/s11069-013-0681-3>
- Harbitz, C. B., Løvholt, F., Pedersen, G., & Masson, D. G. (2006). Mechanisms of tsunami generation by submarine landslides: A short review. *Norwegian Journal of Geology/Norsk Geologisk Forening*, 86(3).
- Haugen, K. B., Løvholt, F., & Harbitz, C. B. (2005). Fundamental mechanisms for tsunami generation by submarine mass flows in idealised geometries. *Marine and Petroleum Geology*, 22(1–2), 209–217. <https://doi.org/10.1016/b978-0-08-044694-3.50022-6>
- Heezen, B. C., & Ewing, W. M. (1952). Turbidity currents and submarine slumps, and the 1929 Grand Banks [Newfoundland] earthquake. *American Journal of Science*, 250(12), 849–873. <https://doi.org/10.2475/ajs.250.12.849>
- Hensen, C., Scholz, F., Nuzzo, M., Valadares, V., Gràcia, E., Terrinha, P., et al. (2015). Strike-slip faults mediate the rise of crustal-derived fluids and mud volcanism in the deep sea. *Geology*, 43(4), 339–342. <https://doi.org/10.1130/G36359.1>
- Higman, B., Shugar, D. H., Stark, C. P., Ekström, G., Koppes, M. N., Lynett, P., et al. (2018). The 2015 landslide and tsunami in Taan Fiord, Alaska. *Scientific Reports*, 8(1), 1–12. <https://doi.org/10.1038/s41598-018-30475-w>
- Hungr, O., Corominas, J., & Eberhardt, E. (2005). Estimating landslide motion mechanism, travel distance and velocity. In *Landslide risk management* (pp. 109–138). CRC Press. <https://doi.org/10.1201/9781439833711-7>
- Hunt, J., Tappin, D., Watt, S., Susilohadi, S., Novellino, A., Ebmeier, S., et al. (2021). Submarine landslide megablocks show half of Anak Krakatau Island failed on December 22nd, 2018. *Nature Communications*, 12(1), 1–15. <https://doi.org/10.1038/s41467-021-22610-5>
- Kajjura, K. (1963). The leading wave of a tsunami. *Bulletin of the Earthquake Research Institute*, 41, 535–571.
- Kim, J., Løvholt, F., Issler, D., & Forsberg, C. F. (2019). Landslide material control on tsunami genesis—The Storegga slide and tsunami (8,100 Years BP). *Journal of Geophysical Research: Oceans*, 124(6), 3607–3627. <https://doi.org/10.1029/2018JC014893>
- Lario, J., Luque, L., Zazo, C., Goy, J. L., Spencer, C., Cabero, A., et al. (2010). Tsunami vs. storm surge deposits: A review of the sedimentological and geomorphological records of extreme wave events (EWE) during the Holocene in the Gulf of Cadiz, Spain. *Zeitschrift für Geomorphologie, Supplementary Issues*, 54(3), 301–316. <https://doi.org/10.1127/0372-8854/2010/0054S3-0029>
- Llave, E., Matias, H., Hernández-Molina, F. J., Ercilla, G., Stow, D. A., & Medialdea, T. (2011). Pliocene–Quaternary contourites along the northern Gulf of Cadiz margin: Sedimentary stacking pattern and regional distribution. *Geo-Marine Letters*, 31(5–6), 377–390. <https://doi.org/10.1007/s00367-011-0241-3>
- Locat, J., & Lee, H. J. (2002). Submarine landslides: Advances and challenges. *Canadian Geotechnical Journal*, 39(1), 193–212. <https://doi.org/10.1139/t01-089>
- Lo Iacono, C., Gràcia, E., Zaniboni, F., Pagnoni, G., Tinti, S., Bartolomé, R., et al. (2012). Large, deepwater slope failures: Implications for landslide-generated tsunamis. *Geology*, 40(10), 931–934. <https://doi.org/10.1130/g33446.1>
- Løvholt, F., Bondevik, S., Laberg, J. S., Kim, J., & Boylan, N. (2017). Some giant submarine landslides do not produce large tsunamis. *Geophysical Research Letters*, 44(16), 8463–8472. <https://doi.org/10.1002/2017GL074062>
- Løvholt, F., Glimsdal, S., & Harbitz, C. B. (2020). On the landslide tsunami uncertainty and hazard. *Landslides*, 17(10), 2301–2315.
- Løvholt, F., Harbitz, C. B., & Haugen, K. B. (2005). A parametric study of tsunamis generated by submarine slides in the Ormen Lange/Storegga area off Western Norway. In *Ormen Lange—An integrated study for safe field development in the Storegga submarine area* (pp. 219–231). Elsevier.
- Løvholt, F., Pedersen, G., & Gislser, G. (2008). Oceanic propagation of a potential tsunami from the La Palma Island. *Journal of Geophysical Research*, 113(C9).
- Løvholt, F., Pedersen, G., Harbitz, C. B., Glimsdal, S., & Kim, J. (2015). On the characteristics of landslide tsunamis. *Philosophical Transactions of the Royal Society A*, 373(2053), 20140376.
- Løvholt, F., Pedersen, G. K., & Glimsdal, S. (2010). Coupling of dispersive tsunami propagation and shallow water coastal response. *Open Oceanography Journal, Caribbean Waves Special Issue*, 4, 71–82. <https://doi.org/10.2174/1874252101004010071>
- Løvholt, F., Schulten, I., Mosher, D., Harbitz, C. B., & Krastel, S. (2018). Modelling the 1929 Grand Banks slump and landslide tsunami. *Geological Society, London, Special Publications*, 477, 315–331. <https://doi.org/10.1144/SP477.28>
- Martínez-Loriente, S., Sallarès, V., & Gràcia, E. (2021). The horseshoe abyssal plain thrust could be the source of the 1755 Lisbon earthquake and tsunami. *Communications Earth & Environment*, 2(1), 1–9. <https://doi.org/10.1038/s43247-021-00216-5>
- Martínez-Loriente, S., Sallarès, V., Gràcia, E., Bartolomé, R., Dañoibeitia, J. J., & Zitellini, N. (2014). Seismic and gravity constraints on the nature of the basement in the Africa-Eurasia plate boundary: New insights for the geodynamic evolution of the SW Iberian margin. *Journal of Geophysical Research: Solid Earth*, 119(1), 127–149. <https://doi.org/10.1002/2013JB010476>
- Masson, D., Harbitz, C., Wynn, R., Pedersen, G., & Løvholt, F. (2006). Submarine landslides: Processes, triggers and hazard prediction. *Philosophical Transactions of the Royal Society A: Mathematical, Physical & Engineering Sciences*, 364(1845), 2009–2039. <https://doi.org/10.1098/rsta.2006.1810>
- Mencaroni, D., Urgeles, R., Camerlenghi, A., Llopart, J., Ford, J., Sanchez Serra, C., et al. (2020). Interaction between contour currents and submarine canyons: Depositional products and significance for mass-wasting processes, Gulf of Cadiz, NE Atlantic. *Sedimentology*.
- Omira, R., Ramalho, I., Terrinha, P., Baptista, M. A., Batista, L., & Zitellini, N. (2016). Deep-water seamounts, a potential source of tsunami generated by landslides? The Hirondele Seamount, NE Atlantic. *Marine Geology*, 379, 267–280. <https://doi.org/10.1016/j.margeo.2016.06.010>
- Paris, A., Okal, E. A., Guérin, C., Heinrich, P., Schindelé, F., & Hébert, H. (2019). Numerical modeling of the June 17, 2017 landslide and tsunami events in Karrat Fjord, West Greenland. *Pure and Applied Geophysics*, 176(7), 3035–3057. <https://doi.org/10.1007/s00024-019-02123-5>
- Pedersen, G., & Løvholt, F. (2008). *Documentation of a global Boussinesq solver. Preprint series. Mechanics and applied mathematics*. Retrieved from <http://urn.nb.no/URN:NBN:no-23418>
- Piper, D. J., Cochonat, P., & Morrison, M. L. (1999). The sequence of events around the epicentre of the 1929 Grand Banks earthquake: Initiation of debris flows and turbidity current inferred from sidescan sonar. *Sedimentology*, 46(1), 79–97. <https://doi.org/10.1046/j.1365-3091.1999.00204.x>
- Posamentier, H. (2001). Lowstand alluvial bypass systems: Incised vs. unincised. *AAPG Bulletin - AAPG BULL.*, 85, 1771–1793. <https://doi.org/10.1306/8626D06D-173B-11D7-8645000102C1865D>
- Rauter, M., Viroulet, S., Gylfadottir, S., Fellin, W., & Løvholt, F. (2022). Granular porous landslide tsunami modelling – The 2014 Lake Askja flank collapse. *Nature Communications*, 13, 678. <https://doi.org/10.1038/s41467-022-28296-7>
- R-Core-Team (2012). *R: A language and environment for statistical computing*. R Foundation for Statistical Computing. Retrieved 2016-04-11, from <http://www.R-project.org/>
- Ren, Z., Zhao, X., & Liu, H. (2019). Numerical study of the landslide tsunami in the South China Sea using Herschel-Bulkley rheological theory. *Physics of Fluids*, 31(5), 056601.

- Rodero, J., Pallarés, L., & Maldonado, A. (1999). Late quaternary seismic facies of the Gulf of Cadiz Spanish margin: Depositional processes influenced by sea-level change and tectonic controls. *Marine Geology*, 155(1), 131–156. [https://doi.org/10.1016/S0025-3227\(98\)00144-3](https://doi.org/10.1016/S0025-3227(98)00144-3)
- Salmanidou, D., Guillas, S., Georgiopolou, A., & Dias, F. (2017). Statistical emulation of landslide-induced tsunamis at the Rockall Bank, NE Atlantic. *Proceedings of the Royal Society A: Mathematical, Physical & Engineering Sciences*, 473(2200), 20170026. <https://doi.org/10.1098/rspa.2017.0026>
- Salmanidou, D., Heidarzadeh, M., & Guillas, S. (2019). Probabilistic landslide-generated tsunamis in the Indus Canyon, NW Indian Ocean, using statistical emulation. *Pure and Applied Geophysics*, 176(7), 3099–3114. <https://doi.org/10.1007/s00024-019-02187-3>
- Sawyer, D. E., Flemings, P. B., Buttles, J., & Mohrig, D. (2012). Mudflow transport behavior and deposit morphology: Role of shear stress to yield strength ratio in subaqueous experiments. *Marine Geology*, 307, 28–39. <https://doi.org/10.1016/j.margeo.2012.01.009>
- Schambach, L., Grilli, S., Tappin, D., Gangemi, M., & Barbaro, G. (2020). New simulations and understanding of the 1908 Messina tsunami for a dual seismic and deep submarine mass failure source. *Marine Geology*, 421, 106093. <https://doi.org/10.1016/j.margeo.2019.106093>
- Schambach, L., Grilli, S. T., & Tappin, D. R. (2021). New high-resolution modeling of the 2018 Palu tsunami, based on Supershear earthquake mechanisms and mapped coastal landslides, supports a dual source. *Frontiers of Earth Science*, 8. <https://doi.org/10.3389/feart.2020.598839>
- Schulten, I., Mosher, D. C., Piper, D. J., & Krastel, S. (2019). A massive slump on the St. Pierre Slope, a new perspective on the 1929 Grand Banks submarine landslide. *Journal of Geophysical Research: Solid Earth*. <https://doi.org/10.1029/2018jb017066>
- Snelling, B., Neethling, S., Horsburgh, K., Collins, G., & Piggott, M. (2020). Uncertainty quantification of landslide generated waves using Gaussian process emulation and variance-based sensitivity analysis. *Water*, 12(2), 416. <https://doi.org/10.3390/w12020416>
- Stich, D., de Lis Mancilla, F., Pondrelli, S., & Morales, J. (2007). Source analysis of the February 12th 2007, Mw 6.0 Horseshoe earthquake: Implications for the 1755 Lisbon earthquake. *Geophysical Research Letters*, 34(12), L12308. <https://doi.org/10.1029/2007GL030012>
- Stich, D., Mancilla, F. d. L., & Morales, J. (2005). Crust-mantle coupling in the Gulf of Cadiz (SW-Iberia). *Geophysical Research Letters*, 32(13), L12308. <https://doi.org/10.1029/2005GL023098>
- Stich, D., Martín, R., & Morales, J. (2010). Moment tensor inversion for Iberia–Maghreb earthquakes 2005–2008. *Tectonophysics*, 483(3–4), 390–398. <https://doi.org/10.1016/j.tecto.2009.11.006>
- Stow, D. A. V., Hernández-Molina, F. J., & Alvarez Zarkian, C. A. (2013). Expedition 339 Scientists. *Proceedings IODP* (Vol. 339). Integrated Ocean Drilling Program Management International, Inc. <https://doi.org/10.2204/iodp.proc.339.2013>
- Svennevig, K., Dahl-Jensen, T., Keiding, M., Merryman Boncori, J. P., Larsen, T. B., Salehi, S., et al. (2020). Evolution of events before and after the 17 June 2017 rock avalanche at Karrat Fjord, West Greenland—A multidisciplinary approach to detecting and locating unstable rock slopes in a remote arctic area. *Earth Surface Dynamics*, 8(4), 1021–1038. <https://doi.org/10.5194/esurf-8-1021-2020>
- Synolakis, C. E., Bardet, J.-P., Borrero, J. C., Davies, H. L., Okal, E. A., Silver, E. A., et al. (2002). The slump origin of the 1998 Papua New Guinea tsunami. *Proceedings of the Royal Society of London. Series A: Mathematical, Physical and Engineering Sciences*, 458(2020), 763–789. <https://doi.org/10.1098/rspa.2001.0915>
- Tappin, D., Watts, P., & Grilli, S. T. (2008). The Papua New Guinea tsunami of 17 July 1998: Anatomy of a catastrophic event. *Natural Hazards and Earth System Sciences*, 8(2), 243–266. Copernicus Publications on behalf of the European Geosciences Union. <https://doi.org/10.5194/nhess-8-243-2008>
- Terrinha, P., Matias, L., Vicente, J., Duarte, J., Luis, J., et al. (2009). Morphotectonics and strain partitioning at the Iberia–Africa plate boundary from multibeam and seismic reflection data. *Marine Geology*, 267(3–4), 156–174. <https://doi.org/10.1016/j.margeo.2009.09.012>
- Twichell, D. C., Chaytor, J. D., Uri, S., & Buczkowski, B. (2009). Morphology of late quaternary submarine landslides along the US Atlantic continental margin. *Marine Geology*, 264(1–2), 4–15. <https://doi.org/10.1016/j.margeo.2009.01.009>
- Urgeles, R., & Camerlenghi, A. (2013). Submarine landslides of the Mediterranean Sea: Trigger mechanisms, dynamics, and frequency-magnitude distribution. *Journal of Geophysical Research: Earth Surface*, 118(4), 2600–2618. <https://doi.org/10.1002/2013jf002720>
- Urgeles, R., Camerlenghi, A., Ruther, D. C., Fantoni, L., Brückner, N. W., De Pro-Díaz, Y. (2021). Euro-Mediterranean submarine landslide database (EMSS21): Online data. Institut de Ciències del Mar (CSIC). <https://doi.org/10.20350/digitalCSIC/13970>
- Vanneste, M., Løvholt, F., Issler, D., Liu, Z., Boylan, N., Kim, J., et al. (2019). A novel quasi-3d landslide dynamics model: From theory to applications and risk assessment. In *Offshore technology conference*. <https://doi.org/10.4043/29363-ms>
- Venables, W. N., & Ripley, B. D. (2010). In [Nachdr] (Ed.), *Modern applied statistics with S* (p. 4). Springer.
- Vizcaino, A., Gràcia, E., Pallàs, R., Garcia-Orellana, J., Escutia, C., Casas, D., & Dañobeitia, J. J. (2006). Sedimentology, physical properties and age of mass transport deposits associated with the Marques de Pombal Fault, Southwest Portuguese Margin. *Norwegian Journal of Geology*, 86, 173–182.
- Walter, T. R., Haghghi, M. H., Schneider, F. M., Coppola, D., Motagh, M., Saul, J., et al. (2019). Complex hazard cascade culminating in the Anak Krakatau sector collapse. *Nature Communications*, 10(1), 1–11. <https://doi.org/10.1038/s41467-019-12284-5>
- Yeh, H., Imamura, F., Synolakis, C., Tsuji, Y., Liu, P., & Shi, S. (1993). The Flores island tsunamis. *Eos, Transactions American Geophysical Union*, 74(33), 369–373. <https://doi.org/10.1029/93e000381>
- Yudhicara, Bani, P., & Darmawan, A. (2015). Geothermal system as the cause of the 1979 landslide tsunami in Lembata Island, Indonesia. *Indonesian Journal on Geoscience*, 2(2), 91–99. <https://doi.org/10.17014/ijog.2.2.91-99>
- Zengaffinen, T., Løvholt, F., Pedersen, G. K., & Harbitz, C. B. (2020). *Effects of rotational submarine slump dynamics on tsunami-genesis—new insight from idealized models and the 1929 Grand Banks event* (p. 500). Geological Society Special Publications.
- Zengaffinen, T., Løvholt, F., Pedersen, G. K., & Muhari, A. (2020). Modelling 2018 Anak Krakatoa flank collapse and tsunami—Effect of landslide failure mechanism and dynamics on tsunami generation. *Pure and Applied Geophysics*.
- Zengaffinen-Morris, T. (2021). *Influence of submarine landslide failure and flow on tsunami genesis* (pp. 67–130). PhD thesis at the University of Oslo. Retrieved from <https://www.duo.uio.no/handle/10852/85503>
- Zengaffinen-Morris, T. (2022). Publication dataset for the paper “on the inference of tsunami uncertainties from landslide run-out observations”. [Data Set]. Retrieved from <https://www.ngi.no/eng/Services/Technical-expertise/Tsunamis/On-the-inference-of-tsunami-uncertainties-from-landslide-run-out-observations-publication-data>
- Zitellini, N., Chierici, F., Sartori, R., & Torelli, L. (1999). The tectonic source of the 1755 Lisbon earthquake and tsunami. *Annals of Geophysics*, 42(1). <https://doi.org/10.4401/ag-3699>
- Zitellini, N., Gràcia, E., Matias, L., Terrinha, P., Abreu, M. A., DeAlteris, G., et al. (2009). The quest for the Africa–Eurasia plate boundary west of the Strait of Gibraltar. *Earth and Planetary Science Letters*, 280(1–4), 13–50. <https://doi.org/10.1016/j.epsl.2008.12.005>
- Zitellini, N., Mendes, L. A., Cordoba, D., Danobeitia, J., Nicolich, R., Pellis, G., et al. (2001). Source of 1755 Lisbon earthquake and tsunami investigated. *Eos, Transactions American Geophysical Union*, 82(26), 285–291.
- Zitellini, N., Rovere, M., Terrinha, P., Chierici, F., Matias, L., & Team, B. (2004). Neogene through quaternary tectonic reactivation of SW Iberian passive margin. *Pure and Applied Geophysics*, 161(3), 565–587. <https://doi.org/10.1007/s00024-003-2463-4>